GEM NEWS INTERNATIONAL

Contributing Editors
Gagan Choudhary, *IIGJ-Research & Laboratories Centre, Jaipur, India* (gagan.choudhary@iigjrlc.org)
Guanghai Shi, *School of Gemmology, China University of Geosciences, Beijing* (shigh@cugb.edu.cn)

COLORED STONES AND ORGANIC MATERIALS

Gemfields emerald and ruby auctions. In May and June 2024, GIA was able to attend viewings of rough gemstones prior to Gemfields auctions in Bangkok. The first viewing offered emeralds from Gemfields' Kagem mine in Zambia, and the second featured rubies from the MRM mine in Mozambique (figure 1). Both viewings were immediately followed by the tender, where bids were submitted online and the winners of each parcel were notified.

Many international buyers attended the auctions, with strong interest from Indian and Israeli companies in the emeralds, while Thai and Indian companies focused mostly on the rubies. Several firms from Europe, China, and other Asian nations also submitted bids on parcels.

During both auctions, production from recent months was offered in pre-graded parcels. These lots are created by experienced professionals who have often spent decades working with the respective gemstones. The first factor in sorting is the size of the stones. Larger stones usually hold higher value, so these are often in very high demand by companies that specialize in fine single stones. Several substantial emerald crystals were available, including one that weighed 479 g (figure 2).

While these exceptional specimens stand out, the true power of skilled gemstone sorting is evident in the larger parcels. Emerald quality is determined by the richness of green color and the clarity (figure 3). When inspecting rubies, color is the most important factor, with different grades assigned based on the intensity of color, the orientation of color, and secondary color components (orangy or purplish). In the case of Mozambique rubies, the color ranges broadly from bright, intense pinkish red to a darker, more "closed" burgundy red (figure 4). Inclusions, especially dense silky bands, bring an extra dimension to ruby grading. This precise grading results in parcels that contain similar-looking finished gemstones in terms of color, size, or both. In some cases, fine gemstones of similar quality but different sizes are offered together because they would create a perfectly matched set (e.g., a larger stone suitable for a ring with two matching earrings and a necklace layout featuring smaller stones).

All products are offered untreated, with the exception of oiling. Oil is routinely used to inspect rough because it can minimize surface reflections and allow better observation of the clarity of the rough gems. While oil generally does not penetrate deep into fractures as it does during intentional fracture-filling treatment, rough buyers typically deep-clean the rough before starting the manufacturing process. All of these rubies are untreated. (Gemfields previously offered some treated parcels but discontinued this practice a few years ago.)

Rough emerald valuation is complex because of the abundant fractures that run through a crystal, and a single crystal will often result in many polished emeralds. This is especially true for the larger pieces of rough emerald. With rubies, a single piece of rough usually results in a single finished gem.

The seemingly unremarkable parcel shown in figure 3 attracted significant attention at the emerald auction. At first sight, this parcel might be overlooked due to the small size of the stones, with some as small as 0.5 g. But on closer examination, all of these stones were unusually clean and had a rich color; such emeralds are very rare and in high demand. This 500 g parcel could be turned into exceptional faceted emeralds.

At these high-stakes auctions, winning or losing a parcel can be determined by variations as small as 0.5% of the total price. While single stones of notable size gather the highest price per carat, the economic impact of larger parcels of smaller gems is often greater. These parcels re-

Editors' note: Interested contributors should send information and illustrations to Stuart Overlin at soverlin@gia.edu.

GEMS & GEMOLOGY, VOL. 60, NO. 3, pp. 400–429.

© 2024 Gemological Institute of America

Figure 1. Fine emerald (>60 ct) and ruby (13 ct) crystals offered at the 2024 Gemfields auctions in Bangkok. Photos by Wim Vertriest.

quire much more manufacturing time (and cost), and the profits gained from them are often needed to keep cutting workshops in operation. Missing out on a large parcel could result in the suspension of manufacturing operations, potentially leading to the loss of the valuable skilled labor required to optimize the rough-to-cut process.

During the event, buyers are allowed a specific time slot to inspect stones. This often involves an entire team of specialists, including heat treaters, preformers, and polishers. The final value of a stone will be determined by its color, shape, and size. Cutting, especially the preforming, is the most important aspect of this process. Experienced cutters assist the company owners by offering input on

Figure 2. Large emerald crystals from the Kagem mine in Zambia. The three crystals have a combined weight of 106 g, while the large single crystal weighs 479 g. In these stones, visible fractures and inclusions will determine how the pieces are processed into smaller preforms before going to polishing. Photos by Wim Vertriest.

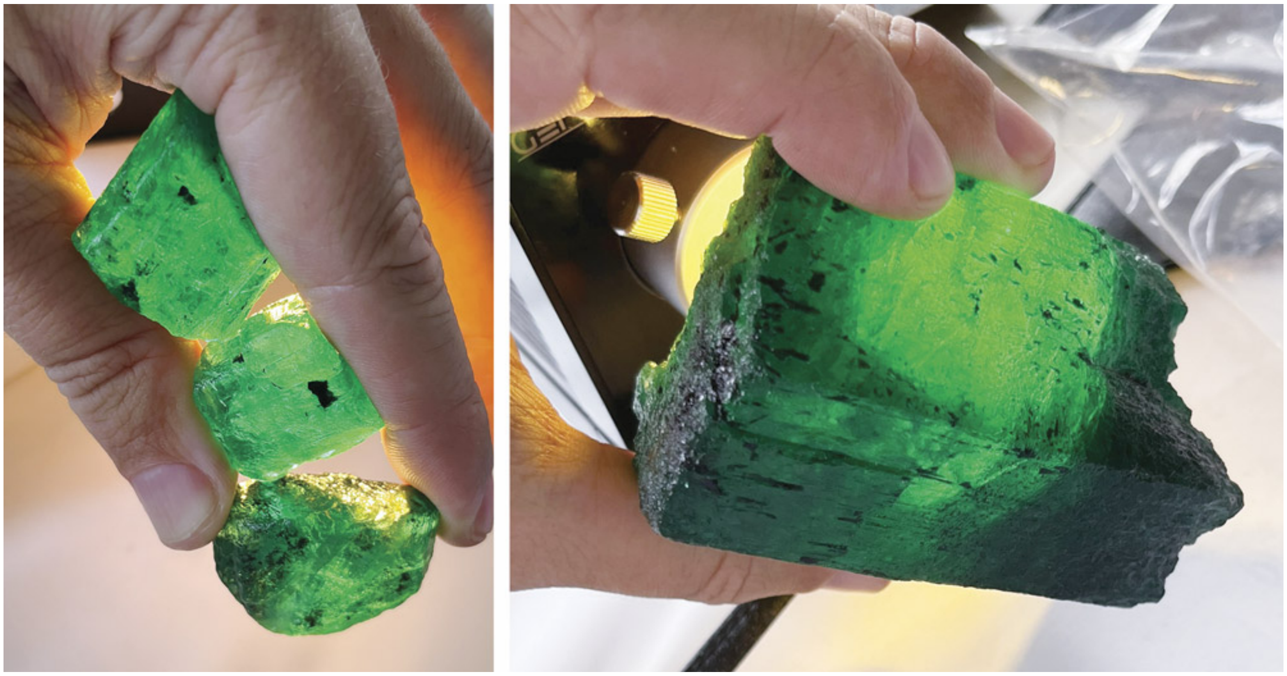

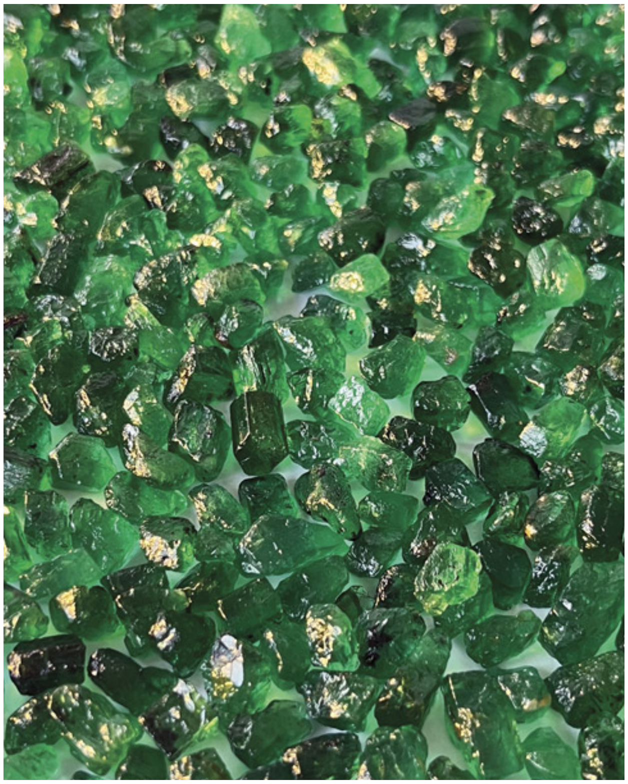

Figure 3. Large parcel of smaller emeralds of very high clarity; the average size of the crystals is between 2.8 and 4 mm. Photo by Wim Vertriest.

Figure 4. Range of rubies produced by the MRM mine in Mozambique: pinkish red material (top, 3.5–5.0 ct) and darker, more "closed" red rubies (bottom, 2.5–3.5 ct). Photos by Wim Vertriest.

what can be done with a piece of rough. For example, the same crystal could yield a 4 ct pear shape or a 3.5 ct cushion. Making such decisions is crucial because the final price of the fashioned gem will be different. This difference must be reflected in the bid placed on the parcel. Considering that certain parcels consist of a few hundred stones, this is a painstaking exercise where minute details can tip the scales one way or another.

Another aspect of valuing the rough involves the impact of potential treatment. The extent of fracture filling can affect the value of an emerald and must be taken into account. The price premium for an untreated stone must be weighed against the value of a stone with a cleaner look from a certain degree of fracture filling or improvement in color due to heating during the manufacturing process. Many buyers are aware that certain grades of ruby will require treatment to improve the color (e.g., rubies with a strong purple tint). The final ruby color is an enormous value factor, which is why a heat treatment expert is often part of the decision-making team at the ruby auction. Striking the right balance between improved color and the price premium for an untreated stone becomes more complex with every auction.

During the May–June tenders, Gemfields offered high-quality rubies and medium- to high-quality rubies. The ruby sales totaled nearly US$69 million, with 97% of the offered goods finding a buyer. The emerald sale included only higher quality rough and totaled US$35 million, with 93% of the lots offered sold.

Wim Vertriest
GIA, Bangkok

Arzakite inclusion in ruby from Mogok. Rubies with intense color and high transparency, such as those from the Mogok mining district in Myanmar, form in metamorphosed carbonate platforms during the retrograde metamorphism stage. This occurs at temperatures of ~620°–670°C and pressures of ~2.6–3.3 kbar (V. Garnier et al., "Marble-hosted ruby deposits from central and southeast Asia: Towards a new genetic model," *Ore Geology Reviews*, Vol. 34, 2008, pp. 169–191). The protolith comprises carbonates enriched in detrital Fe-Cr-V-bearing clays, shales with organic matter, and intercalated evaporitic layers.

Previous studies of primary fluid inclusions trapped by ruby at Mogok (G. Giuliani et al., "Fluid inclusions in ruby from Asian marble deposits: Genetic implications," *European Journal of Mineralogy*, Vol. 27, 2015, pp. 393–404) indicated the contemporary trapping of two carbonic immiscible fluid inclusions: mono- to two-phase fluid inclusions in the CO_2-H_2S ± COS ± S_8 ± H_2O system and multi-solid carbonic fluid inclusions in the Na-K-Ca-CO_3-SO_4-NO_3-Cl-F-(CO_2-H_2S) system. The multiple solids are mainly mixtures of Na-Ca-Al-carbonates (such as shortite and dawsonite), sulfates, phosphates, nitrates, fluorides, and chlorides (such as halite). They are the trapped recrystallized residues of molten salts formed during the metamorphism of evaporitic lenses (chlorides and sulfates) intercalated in the carbonate-shale rocks. The carbon dioxide is released by devolatilization of the original limestones during metamorphism. H_2S originated from the partial or total dissolution of evaporites and subsequent sulfate reduction by organic carbon, which produced graphite and pyrite. The formation of pyrite sequestered iron and led to the formation of iron-poor ruby.

In 2018, American Gemological Laboratories examined a 33.98 ct freeform carved ruby cabochon from Mogok measuring 24.08 × 18.48 × 8.30 mm (figure 5, left). The medium-quality, semitransparent to translucent stone was heavily included with numerous small cavities and whitish fillers on the base (figure 5, right). Energy-dispersive X-ray fluorescence analysis (in wt.% oxide) revealed low trace concentrations of gallium (0.004), iron (0.020), and titanium (0.026), with higher vanadium (0.071) and chromium (0.607). A large and highly reflective, soft yellowish syngenetic inclusion, measuring about 0.5 × 0.2 mm, was evident on the base (figure 5, right). Raman analysis of the inclusion, taken with 514 nm laser excitation, gave a spectrum (figure 6) that we compared to a couple of samples from the RRUFF database and the Raman data of arzakite intimately associated with graphite in nodules of tsavorite from the Scorpion mine in Kenya (R. Thomas et al., "Genetic significance of the 867 cm^{-1} out-of-plane Raman mode in graphite associated with V-bearing green grossular," *Mineralogy and Petrology*, Vol. 112, 2018, pp. 633–645). The best match identified it as arzakite, with Raman peaks at 210, 275, 390, and 590 cm^{-1}. Fourier-transform infrared analysis also highlighted the presence of diaspore and kaolinite in the ruby.

Arzakite, the sulfohalogenide of mercury ($Hg_3S_2(Br,Cl)_2$), forms a chemical series with lavrentievite ($Hg_3S_2(Cl,Br)_2$), originally reported from the Arzakskoye deposit, Uyuk Range, in the eastern Siberia region of Russia (V.I. Vasil'ev et al., "Lavrentievite and arzakite, new natural mercury sulfohalides," *Geologiya i Geofizika*, Vol. 25, 1984, pp. 54–63). It is a supergene mineral found in rhyolite-dacite porphyries and formed between 100°C and 200°C in relatively near-surface conditions.

Figure 5. The 33.98 ct carved ruby cabochon from Mogok (left) and its highly reflective, soft yellowish arzakite inclusion and whitish fillers on the base (right). Photos by Christopher Smith.

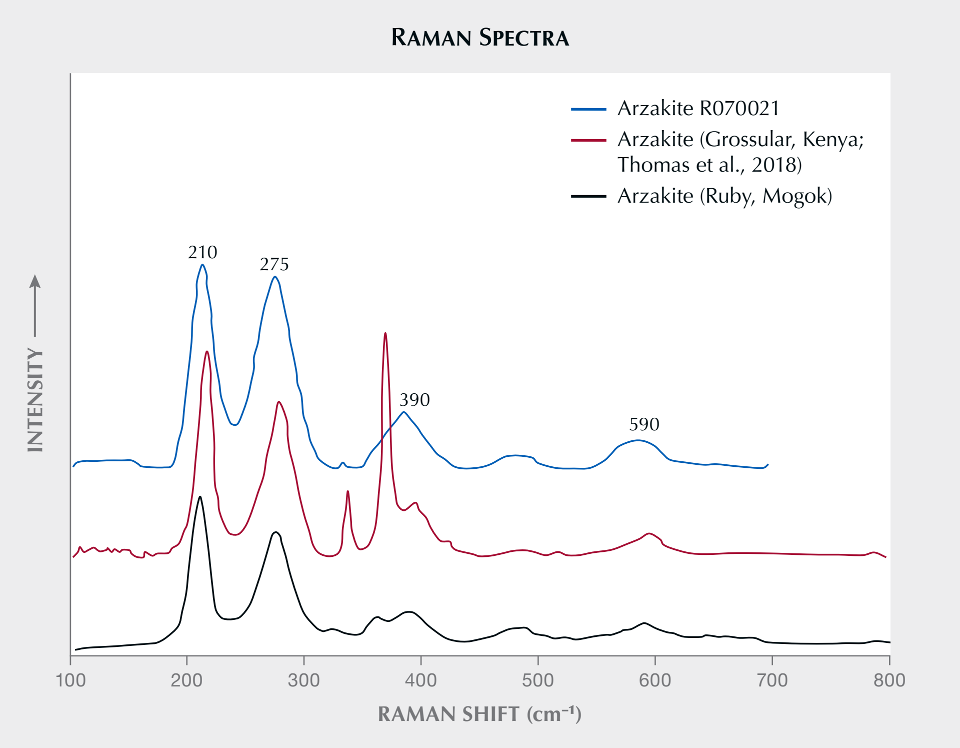

Figure 6. The Raman spectrum (514 nm laser excitation) of an arzakite inclusion in a ruby from Mogok. These peak positions are similar to those observed for an arzakite inclusion in a green grossular (tsavorite) from Kenya by Thomas et al. (2018) and a RRUFF reference spectrum.

The nature and chemical composition of inclusions and fluids associated with ruby in marble from Mogok highlighted the formation of sulfurous fluids and/or molten salts in a closed system with low fluid mobility. The Na–K–Ca–Li–CO_3–SO_4–NO_3–Cl–F fluid systems are powerful fluxes that lowered the temperature of chloride- and fluoride-rich ionic liquids. They provided transport over a very short distance of aluminum and/or silica and transition metals (Cr-V) contained in phengites and organic matter included in anhydrite and salts during prograde metamorphism. The presence of organic matter associated with evaporites is key for the formation of arzakite and sulfides. Evaporites played the role of fluxes, resulting in the formation of an alkaline saline magma in a closed system, much like a pressure cooker, where all the needed ingredients combined at high temperature to extract the chemical elements from the initial protoliths with their redistribution according to atomic and chemical compatibility. In these growth conditions, volatile elements such as mercury cannot escape from the system and (with sulfur) may preferentially form a new stable mineral. The halogens bromine and chlorine of arzakite, elements that are conservative in solution, originated from the evaporites, especially salts as halite (figure 7).

In nature, mercury is known to accumulate in sedimentary contexts (i.e., fluid mud and/or organic matter), especially with organic carbon. Some black shales present anomalous mercury concentrations associated with polymetallic sulfide-rich shales (R. Yin et al., "Anomalous mercury enrichment in Early Cambrian black shales of South China: Mercury isotopes indicate a seawater source," *Chemical Geology*, Vol. 467, 2017, pp. 159–167). Mercury can be used as a proxy to understand the formation of sulfide-rich shales. In the case of South China, a seawater origin is advanced to explain the anomalous mercury contents observed in the black shales (178–505 ppb) and the polymetallic sulfide-rich samples (10900–20700 ppb). These contexts of mercury accumulation also match with arzakite's sedimentary environment. However, mercury is very sensitive to temperature, and arzakite in the present case is a high-temperature metamorphic mineral. According to previous studies showing mercury contents in sedimentary rocks, all the mercury should be degassed by 650°C (B. Marie et al., "Determination of mercury in one hundred and sixteen geological and environmental reference materials using a direct mercury analyser," *Geostandards and Geoanalytical Research*, Vol. 39, 2015, pp. 71–86). The only way to preserve mercury during such an amphibolite metamorphism event is to attain a closed system, in this case with the fusion of evaporites.

This is the first time a Hg-S-bearing inclusion has been described in ruby. The presence of arzakite is a product of the genesis of ruby in marbles, in which the metamorphism of the sedimentary protolith occurred at very high temperature in a closed system where fluids could not escape. The fusion of the mixture of the protolith nucleated an alkaline-salty magma where all the chemical elements combined, forming ruby and minerals such as arzakite.

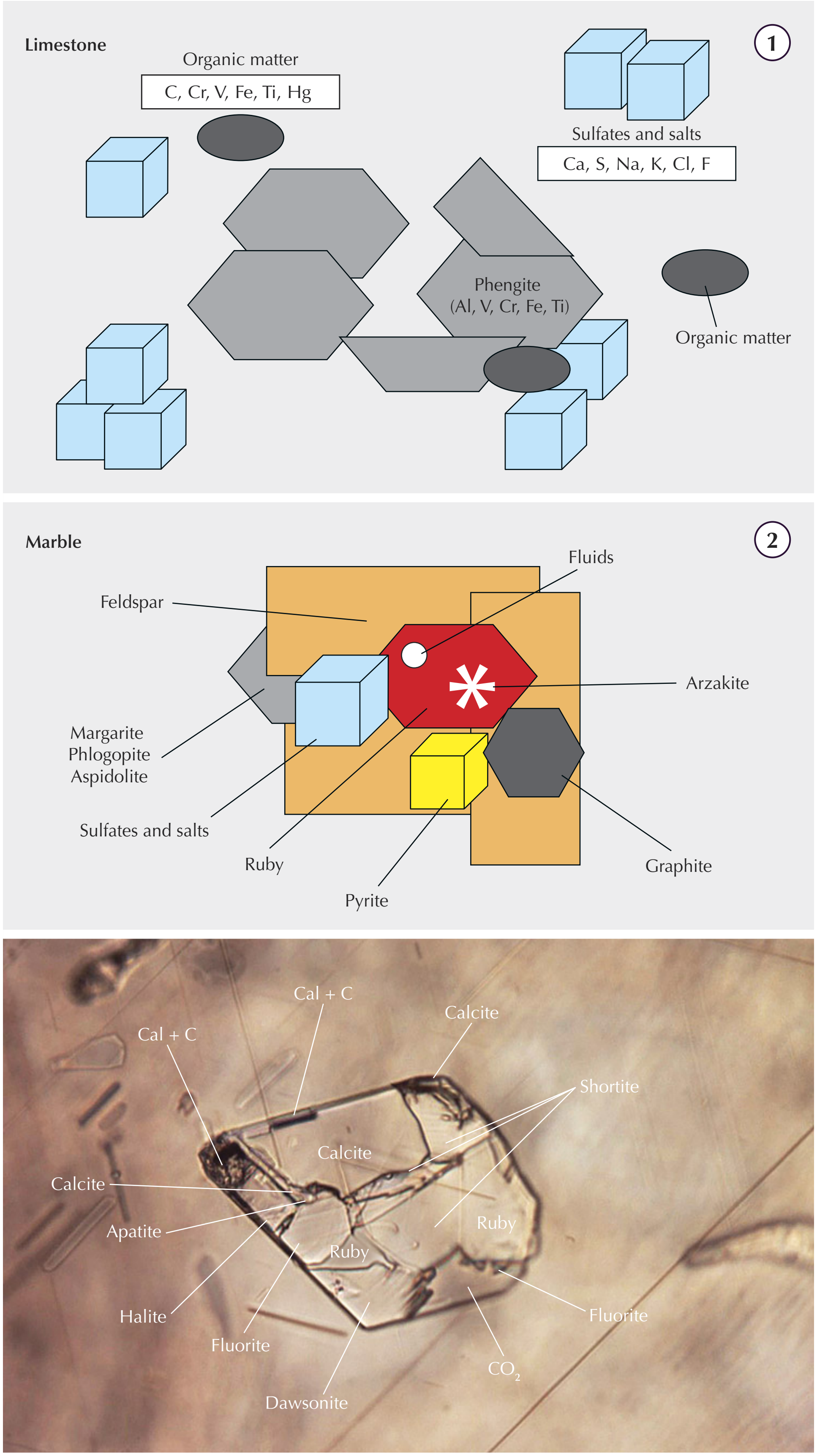

Figure 7. The model of formation of ruby deposits from the sedimentary stage of the protolith with the deposition of carbonates, dolomitic carbonates, organic matter–bearing shale, and marine and non-marine evaporites (stage 1) to the Himalayan metamorphism of the ruby protolith (stage 2); modified from Garnier et al. (2008). The arzakite inclusion is contained in ruby. The photomicrograph on the bottom shows a molten salts–bearing fluid inclusion in ruby with inclusions of calcite (Cal), graphite (C), apatite, halite, fluorite, dawsonite, shortite, and a CO_2-H_2S-bearing fluid phase (CO_2). Photomicrograph by Gaston Giuliani; field of view 0.49 mm.

This finding underscores the importance of detailed inclusion studies offering critical insights into the formation of gems such as Mogok ruby.

Gaston Giuliani
Université Paul Sabatier, Toulouse, France
Université de Lorraine, CRPG/CNRS, Vandœuvre-lès-Nancy, France

Christopher P. Smith
American Gemological Laboratories (AGL), New York

Julien Boulliung
Université de Lorraine, CRPG/CNRS

Zoned trapiche emerald with goshenite overgrowth. GIA's Tokyo laboratory recently examined a 12.62 ct trapiche emerald with areas of the near-colorless beryl variety goshenite (figure 8). The stone was carved in the shape of a modified hexagram measuring 23.66 × 19.65 × 5.66 mm.

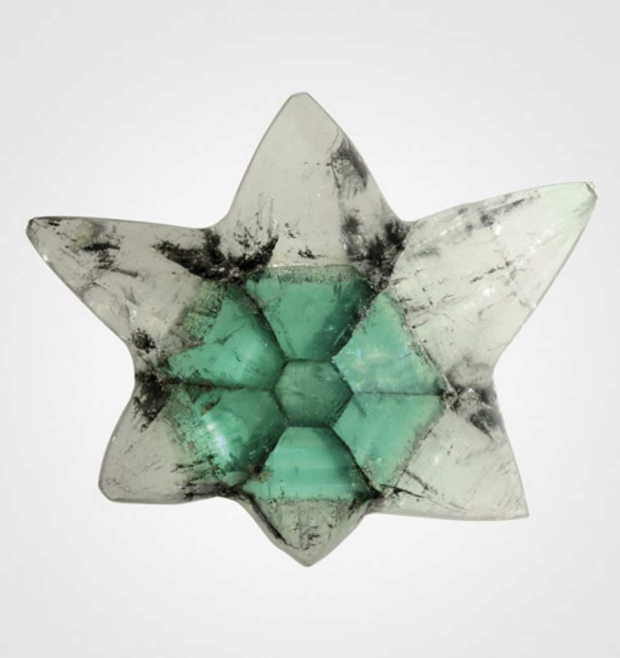

Figure 8. A 12.62 ct trapiche emerald with areas of near-colorless goshenite. Photo by Shunsuke Nagai.

The internal features consisted of tubes, graphite, and jagged three-phase inclusions composed of a cube of halite (NaCl), a carbon dioxide (CO_2) gas bubble, and water (H_2O). Both the green and the near-colorless areas showed similar Raman spectra consistent with a beryl structure and spot refractive index readings of 1.57, matching that of beryl. The nearly identical Raman spectra patterns and intensity ratios indicated that the crystal axes of both areas were aligned. Some of the inclusions such as tubes were also in agreement with the internal fibrous growth structure of both the green and the near-colorless arm areas. These points suggested that both green and near-colorless arms were almost in the same crystallographic direction (figure 9).

The green core and green arms showed hexagonal weak green color bands. Absorption lines and bands related to trivalent vanadium (V^{3+}) and chromium (Cr^{3+}) were detected by a handheld spectroscope and an ultraviolet/visible absorption spectrometer in the green area but not in the near-colorless area. Chemical analyses using energy-dispersive X-ray fluorescence (EDXRF) demonstrated that the green trapiche area was consistent with a Colombian origin and the near-colorless goshenite area was poorer in minor elements of sodium, magnesium, vanadium, chromium, and iron while richer in potassium and cesium than the green core and arms (table 1). (The behavior of rubidium is unknown with this chemical measurement method.)

Next, we considered the processes that might have formed such a zoned trapiche emerald. The finest trapiche emeralds are found in the Colombian deposits on the western side of the Eastern Cordillera Basin (e.g., Muzo, Coscuez, and Peñas Blancas), characterized by folding and thrusting along tear faults at the time of the Eocene-Oligocene boundary between 38 and 32 million years ago. Accumulation of hot H_2O-NaCl-CO_2 fluids at the tip of décollement faults in black shale host rock led to maximum fluid overpressure and subsequent sudden decompression associated with the collapsing of rock, forming emerald-bearing vein systems. The rapid growth of trapiche arms

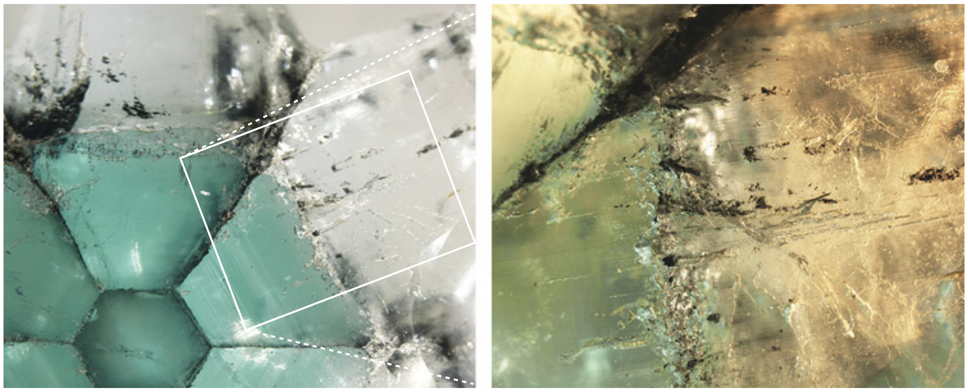

Figure 9. Left: Green color banding in the green internal arm areas of the trapiche emerald; field of view 1.18 cm. Right: Black and whitish inclusions in the green and near-colorless areas; field of view 5.95 mm. Photomicrographs by Makoto Miura (left) and Taku Okada (right).

TABLE 1. Comparison of chemical compositions (in wt.%) of the trapiche emerald and goshenite areas by EDXRF[a] and partial molar volumes of ions in water.

Area	SiO_2	Al_2O_3	Cr_2O_3	Fe_2O_3	V_2O_3	MgO	Na_2O	K_2O	Rb_2O	Cs_2O
Trapiche emerald	67.77 (19)	16.00 (12)	0.145 (9)	0.159 (5)	0.200 (10)	0.82 (7)	0.87 (11)	0.039 (3)	0.0003 (2)	0.001 (6)
Goshenite	68.09 (19)	16.71 (12)	0.006 (2)	0.054 (3)	0.009 (3)	0.39 (6)	0.65 (10)	0.078 (3)	0.0001 (1)	0.010 (5)
	Si^{4+}	Al^{3+}	Cr^{3+}	Fe^{3+}	V^{3+}	Mg^{2+}	Na^+	K^+	Rb^+	Cs^+
Partial molar volume (cm^3/mol)[b]	na[c]	na	–36.7[d]	–36.5[d]	na	–21.55[e]	–0.87[e]	9.06[e]	14.3[e]	21.42[e]

[a] Chemical compositions were calculated assuming a BeO content of 14 wt.% and the uncertainties are given as least significant figures in parentheses

[b] At infinite dilution at 298 K and 1 bar

[c] na = not available

[d] Swaddle and Mak (1983)

[e] Shock et al. (1997)

was shown to start at the beginning of decompression (e.g., I. Pignatelli et al., "Colombian trapiche emeralds: Recent advances in understanding their formation," Fall 2015 *G&G*, pp. 222–259).

Pignatelli et al. (2015) performed EDX elemental mapping using an electron probe microanalyzer for sodium, magnesium, aluminum, vanadium, and chromium on a trapiche beryl, which consisted of a near-colorless core and arms and green overgrowth areas. The green overgrowth areas were richer in sodium, magnesium, vanadium, and chromium than the near-colorless core and arms. The behavior of these trace elements corresponds to the color and is consistent with our EDXRF results on the present stone, which showed an inverse color distribution. In addition to these trace elements, we examined potassium and cesium and found for the first time that they behaved in a manner opposite to that of sodium, magnesium, vanadium, chromium, and iron.

Such chemical differences could be due to either compositional changes in the incoming fluids themselves in a simple open system or fluid differentiation associated with emerald crystallization in a closed system. Various chemical elements will behave differently to changes in pressure or temperature of the mineralizing aqueous fluid in such a system. For instance, elements such as potassium and cesium, with a so-called positive partial molar volume, will be released from the fluid due to increased pressure and/or decreased temperature (e.g. table 1; T.W. Swaddle and M.K.S. Mak, "The partial molar volumes of aqueous metal cations: Their prediction and relation to volumes of activation for water exchange," *Canadian Journal of Chemistry*, Vol. 61, No. 3, 1983, pp. 473–480; E.L. Shock et al., "Inorganic species in geologic fluids: Correlations among standard molal thermodynamic properties of aqueous ions and hydroxide complexes," *Geochimica et Cosmochimica Acta*, Vol. 61, No. 5, 1997, pp. 907–950). These elements are concentrated in the colorless goshenite areas. On the other hand, V^{3+} and Cr^{3+}, with a so-called negative partial molar volume, would have reacted in the opposite way and are depleted in the goshenite but enriched in the emerald areas, indicating a change in the pressure and/or temperature of the fluid as it crystallized either goshenite or emerald. The classical chemical thermodynamic considerations above may provide insight into the differences in behavior among trace elements and the growth history that zoned gems such as this stone have undergone in fluids or melts.

This trapiche emerald offers a unique example to consider trace element behavior and geological conditions during crystal growth, as well as the diversity of trapiche emerald formation.

Taku Okada and Makoto Miura
GIA, Tokyo

Almandine garnet from Phu Tho, Vietnam. During the early 2000s, garnet was discovered and mined along with black tourmaline and aquamarine in the northern Vietnamese province of Phu Tho. Its undesirable appearance led to a suspension of mining activities, but mining resumed in 2021 with more promising results. Phu Tho borders the province of Yen Bai, which has produced a wide range of gem materials such as ruby, sapphire, spinel, and tourmaline. Despite their proximity, the geological settings are much different, and Phu Tho produces tourmaline, beryl, and garnet.

Rough garnet from Phu Tho possesses typical cubic crystal shapes with either trapezohedral or elongated habit.

Figure 10. The trapezohedral habit of garnet from Phu Tho. The trapezohedral habit is suitable for cutting as cabochons or beads, while the elongated habit (not shown) would be appropriate for carving. Photos by Nguyen Thanh Nhan.

The authors purchased a total of 28 samples, including 26 euhedral trapezohedral crystals (figure 10) and two enormous rough samples, from a garnet miner in Phu Tho. One crystal was cut into a cabochon measuring 17.23 × 14.82 × 9.37 mm and weighing 24.30 ct. The other 25 crystals were kept intact, ranging from 11 to 29 mm with a total weight of 218.58 g. The two large samples were elongated and up to 30 cm in length. Most of the garnet is found in black mica schist. Although the materials formed within the host rock, the crystals can be detached easily into loose crystals. The Phu Tho garnet displays colors from medium dark to very dark red to purple-red. Its transparency ranges from translucent to opaque, with no transparent material found, and the luster is vitreous to greasy.

Standard gemological testing of the samples showed a refractive index of 1.78 to over the limit of the refractometer, specific gravity ranging from 4.01 to 4.12, an almandine spectrum, and an inert reaction under ultraviolet light (long-wave and short-wave). Microscopic examination revealed several solid black inclusions and oriented needles of rutile, some fingerprints, and feathers filled with iron stains. These results confirmed almandine garnet. Raman spectroscopy showed distinct peaks at 123 and 1456 cm^{-1}, consistent with almandine.

Because of their dark tone and low transparency, Phu Tho garnets are more suitable for cutting as cabochons, beads, and ornamental carvings (figure 11). Asterism was observed in several samples from Phu Tho, with four- or six-rayed stars caused by oriented rutile needles intersecting at angles of 120° and 60°. Interestingly, the occurrence of both four- and six-rayed stars within a polished sample is not rare. In the studied samples, we counted a maximum of five six-rayed stars and two four-rayed stars on one side of a garnet. The display of multiple stars within garnet was previously reported by K. Schmetzer et al. (“Star garnets and star garnet cat’s-eyes from Ambatondrazaka, Madagascar,”

Figure 11. Vietnamese garnet from Phu Tho displays a medium dark brown-red, translucent to opaque appearance. The polished octahedral crystal weighs 450 g, the carving weighs 234 g, and the four-rayed star garnet weighs 26 ct. Photo by Pham Minh Tien.

Figure 12. Two views of the 2.43 ct orangy pink morganite with bright yellow and dark brown inclusions lying in a plane. Photos by Sandie Clain, © LFG; courtesy of Gravier & Gemmes.

Journal of Gemmology, Vol. 28, No. 1, 2002, pp. 13–24), and so far this phenomenon has only been found in garnet.

Although most Phu Tho garnet is not suitable for high-quality jewelry making, giant crystals or well-formed crystals on host rock could be valuable as ornamental objects or mineral specimens.

Pham Minh Tien and Nguyen Thanh Nhan
Liu Gemological Research and Application Center (LIULAB)
Ho Chi Minh City

Helvine inclusions in morganite. A group of remarkable bright yellow inclusions in a partially polished 2.43 ct orangy pink morganite from Madagascar (figure 12) recently caught our attention. The beryl was identified by a combination of classical gemology and spectroscopy. The partial hexagonal prism contained hundreds of yellow crystals aligned on a plane. Although it was difficult to evaluate their complex polyhedral morphology, many had triangular faces (figure 13). Using reflected light, several of the crystals were found to reach the surface of a polished face. In addition, a few very dark brown, somewhat elongated crystals were observed in the same plane.

Raman spectra were obtained with a Jobin Yvon T6400 Raman spectrometer, with diode-pumped solid-state (DPSS) laser excitation at 458 and 561 nm, at 2 $\mathrm{cm^{-1}}$ resolution. Three major peaks at about 130, 180, and 890 $\mathrm{cm^{-1}}$ and smaller matching features were observed. These were identified as helvine using the RRUFF database (Lafuente et al., 2015, https://rruff.info/about/downloads/HMC1-30.pdf) and CrystalSleuth software (figure 14). Similar spectra were obtained on three different surface-reaching inclusions using both excitation wavelengths. The dark crystals were identified as hubnerite, $\mathrm{Mn^{2+}(WO_4)}$, also through Raman spectroscopy using the same software, with a dominant band around 882 $\mathrm{cm^{-1}}$.

Because of the very bright color of the yellow inclusions, we attempted to detect their absorption with a visible absorption spectrum. Ultraviolet/visible/near-infrared (UV-Vis-NIR) spectra were acquired over 365–1000 nm using a mobile instrument with an integrating sphere (Magilabs GemmoSphere), with 0.1 seconds acquisition time, 50 accumulations, and spectral resolution of about 1.5 nm. The spectrum presents strong, relatively sharp absorption features at about 420, 446, and 477 nm, with broader bands at about 567 and 830 nm (figure 15). The absorptions at 420, 446, and 477 nm match those for the helvine-genthelvite series documented previously (U. Hålenius, "Absorption of light by exchange coupled pairs of tetrahedrally coordinated divalent manganese in the helvite-genthelvite solid solution," *Periodico di Mineralogia*, Vol. 80, No. 1, 2011, pp. 105–111). Their strong violet and blue absorption induced the vivid yellow color. The features at about 567 nm ($\mathrm{Mn^{3+}}$), 830 nm (iron-related), and 965 nm (water-related) come from the beryl matrix (D.L. Wood and K. Nassau, "The characterization of beryl by visible and infrared absorption spectroscopy," *American Mineralogist*, Vol. 53, No. 5-6, pp. 777–800).

Helvine is a cubic beryllosilicate with the chemical formula $\mathrm{Be_3Mn^{2+}_4(SiO_4)_3S}$. It belongs to the helvine group of minerals, where divalent manganese can be replaced by di-

Figure 13. Bright yellow inclusions with polyhedral shapes, often with triangular faces, accompanied by a small number of very dark brown crystals. Photomicrograph by Aurélien Delaunay; field of view 2.2 mm.

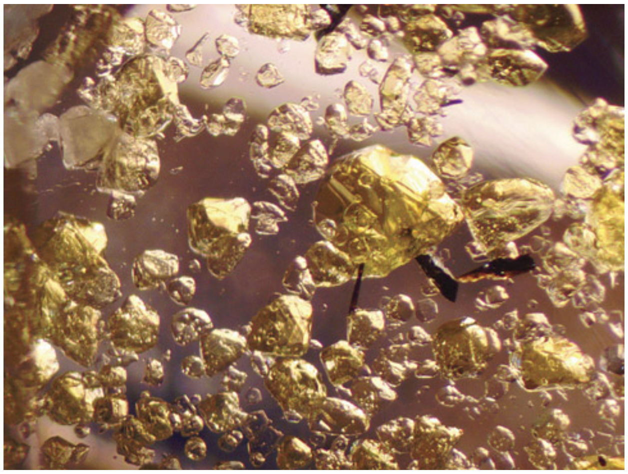

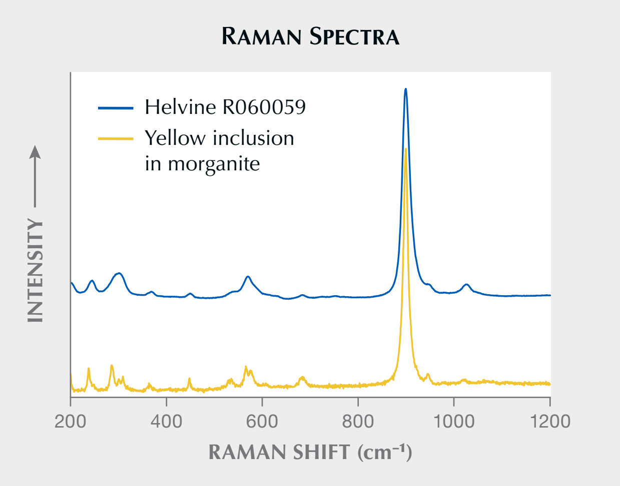

Figure 14. Comparison of the Raman spectrum of the yellow inclusions and the RRUFF reference Raman spectrum for helvine.

valent iron or zinc. Its intrinsic saturated yellow color (the name comes from the Latin *helvus*, for "yellow") is due to exchange-coupled pairs of tetrahedrally coordinated Mn^{2+} ions (Hålenius, 2011). This explains why the color remained strong even with a short optical path in the inclusions. Helvine crystals are usually tetrahedral, thus with only triangular faces, which is consistent with the preliminary visual observations. Yet the morphology was quite different from what is recorded in the Mindat database (https://www.mindat.org/min-40167.html), probably because these inclusions can be considered microcrystals. Small crystals often show fast-growing faces that are absent from larger ones (I. Sunagawa, *Crystals: Growth, Morphology and Perfection*, 2005, Cambridge University Press, Cambridge, UK). Helvine is known to occur in highly complex pegmatites, hence its association with beryl in the present specimen. Hubnerite may sometimes grow within pegmatites as well. Note that helvine and morganite beryl are beryllium-containing. Together with hubnerite, they accommodate manganese (as the coloring agent for morganite). The plane containing these unusual inclusions probably represents a manganese-rich growth spurt, also with tungsten and sulfur.

Figure 15. UV-Vis-NIR absorption spectrum of the morganite containing the helvine inclusions. The helvine-related Mn^{2+} features at 420, 446, and 477 nm cause the inclusions' yellow color, while the Mn^{3+} broad band at around 567 nm provides the pink component to the beryl host. The bands at around 830 and 965 nm are also beryl-related.

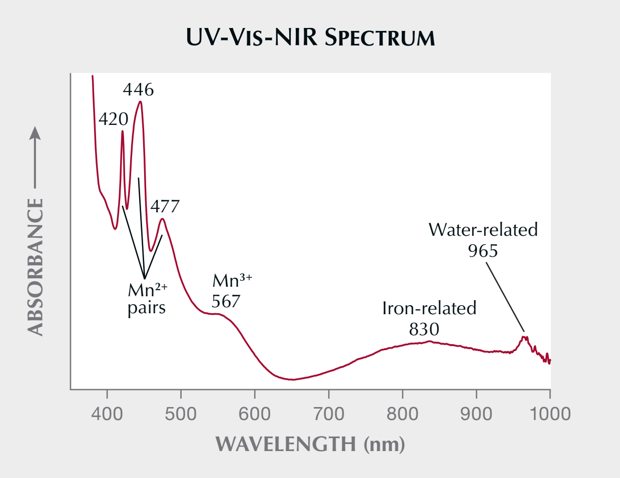

Emmanuel Fritsch (Emmanuel.Fritsch@cnrs-imn.fr)
Nantes Université, CNRS
Institut des Matériaux de Nantes Jean Rouxel (IMN)
Nantes, France

Stefanos Karampelas, Aurélien Delaunay, and Ugo Hennebois
Laboratoire Français de Gemmologie (LFG)
Paris

Mineral assemblage of "Paraíba matrix." Since entering the market in the late 1980s, Paraíba tourmaline has been sought after for its electric blue-green tone. A product called "Paraíba matrix" or "Paraíba in quartz" emerged about three years ago. Two examples of this material, pear-shaped cabochons weighing 4.23 and 3.67 ct (samples PB1 and PB2, respectively), were purchased from the September 2023 Hong Kong Jewellery and Gem Fair (figure 16). The blue minerals in these samples showed an attractive neon-blue color with low clarity surrounded by opaque or transparent white minerals. Dark red minerals were also scattered in the matrix.

Figure 16. Two pieces of "Paraíba matrix" weighing 4.23 ct (sample PB1, left) and 3.67 ct (PB2, right). Photo by Xinchenlu Ai.

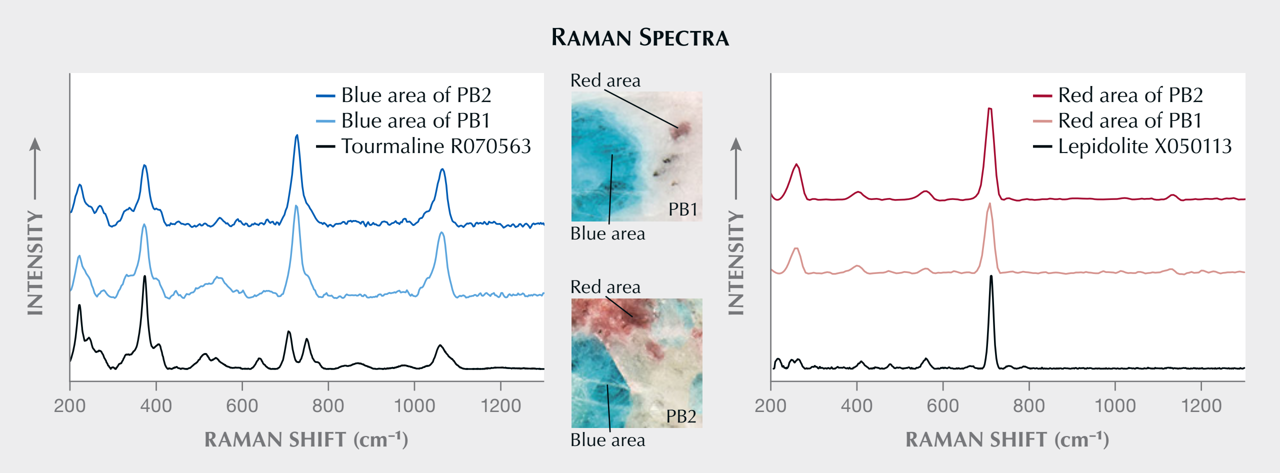

Figure 17. Raman spectra of the embedded blue and dark red minerals in the "Paraíba matrix" samples, with standard RRUFF reference spectra included for comparison. Spectra are offset vertically for clarity.

Raman spectroscopy identified the blue mineral as tourmaline (figure 17, left), and X-ray fluorescence (XRF) spectroscopy showed that it contained copper and manganese. These results, combined with the material's bright neon-blue color, confirmed the blue mineral as Paraíba tourmaline. In both samples, the Paraíba tourmaline displayed color banding, with bluish white cores surrounded by neon-blue rims. The Raman spectra of the dark red mineral in both samples were consistent with that of lepidolite in the RRUFF database (figure 17, right). The Raman spectrum of the opaque white part of PB1 was consistent with albite (figure 18, left), while that of the transparent white part of PB2 was consistent with quartz (figure 18, right).

Based on the Raman and XRF tests of both samples, the "Paraíba matrix" was mainly composed of blue Paraíba tourmaline, dark red lepidolite, opaque white albite, and transparent white quartz. Thus, the white matrix minerals were not all quartz, as suggested by the trade name "Paraíba in quartz." The Paraíba tourmalines in these samples cannot be cut and polished into faceted gemstones due to their low clarity. Cutting and polishing these unique pieces into cabochons can provide more affordable options for fashion jewelry designers and customers.

Xinchenlu Ai and Xiaojing Lai
Gemmological Institute
China University of Geosciences, Wuhan

A minute foraminifera shell in a natural non-nacreous black pearl. Nacre can form around nearly any irritant that infiltrates a shell, resulting at times in pearls with unique internal structures. In very rare cases, foraminifera shell (also known as "test") can serve as the nuclei of pearls produced by different mollusks (Spring 2023 GNI, pp. 143–145). These tiny single-celled marine microorganisms can be found on the seafloor and are usually about half a millimeter to one millimeter long.

Figure 18. Raman spectra of the white matrix in the two "Paraíba matrix" samples, with standard RRUFF reference spectra included for comparison. Spectra are offset vertically for clarity.

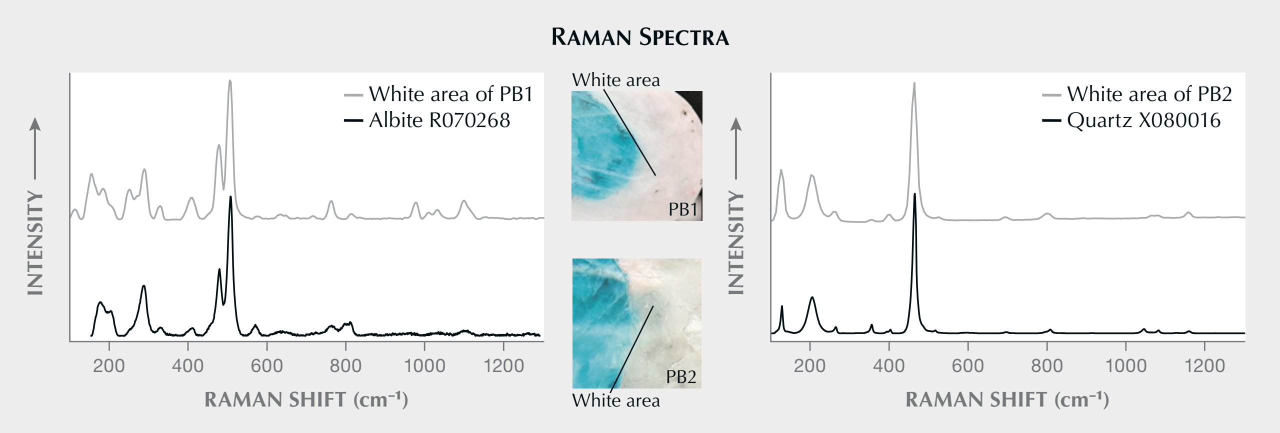

Figure 19. A black non-nacreous pearl measuring 1.55 × 1.43 mm and weighing 0.02 ct. Photo by Gaurav Bera.

GIA's Mumbai laboratory recently received a lot of non-nacreous brown and black pearls of various shapes, collected by a Bahraini diver over a period of six years. The lot was submitted for scientific examination and contained pearls from both the *Pinctada radiata* and *Pinna* species (pen pearls) fished from Bahrain. Real-time X-ray microradiography (RTX) revealed different types of cores and acicular (radial) structures in most of the pearls. One very intriguing structure was observed in a black near-round pearl weighing 0.02 ct and measuring 1.55 × 1.43 mm, reportedly from a *Pinctada radiata* mollusk (figure 19).

The pearl had a glossy appearance with a few pits and no surface-reaching cracks. Viewed under high magnification with a fiber-optic light, it showed a non-nacreous surface, presenting cellular outlines with fine small lines within each cell (figure 20, left). When exposed to X-ray fluorescence, the pearl showed an inert reaction. Energy-dispersive X-ray fluorescence spectrometry revealed a manganese level of 76 ppm and a higher strontium level of 1160 ppm, indicative of a saltwater origin. Under long-wave and short-wave ultraviolet radiation, the pearl showed an inert reaction. However, DiamondView imaging revealed a remarkable cellular structure within. A bluish reaction was observed at the boundaries outlining the cellular columnar structures with thin, short lines within the cells (figure 20, right). This cellular surface structure appeared different from the pseudohexagonal cellular outline found in pen pearls (N. Sturman et al., "Observations on pearls reportedly from the Pinnidae family (pen pearls)," Fall 2014 *G&G*, pp. 202–215). Based on the authors' previous observations, this type of structure is more typically found on the surface of non-nacreous pearls from the *Pinctada radiata* mollusk.

Raman spectroscopy using 514 nm laser excitation was performed on two spots. The first spot revealed peaks at 150 and 280 cm^{-1} with the associated band at 1086 cm^{-1}. The second spot also revealed a peak at 1086 cm^{-1} associated with aragonite and calcite, but there were no other clear peaks to identify which of the two calcium carbonate polymorphs was present in that area of the pearl.

Interestingly, RTX imaging and X-ray computed microtomography (μ-CT) analysis revealed a minute foraminifera shell at the pearl's core, measuring approximately 0.44 × 0.38 mm. The shell exhibited a double thin-walled structure, surrounded by an organic-rich area and an acicular (radial) structure with fine growth arcs crossing it. The radiating acicular structure covered the entire area of the pearl (figure 21, A and C). When observed from the top

Figure 20. Left: Non-nacreous surface of the black pearl; field of view 3.4 mm. Right: DiamondView image showing a bluish reaction of the outline of the cellular structure. Photos by Anukul Belanke.

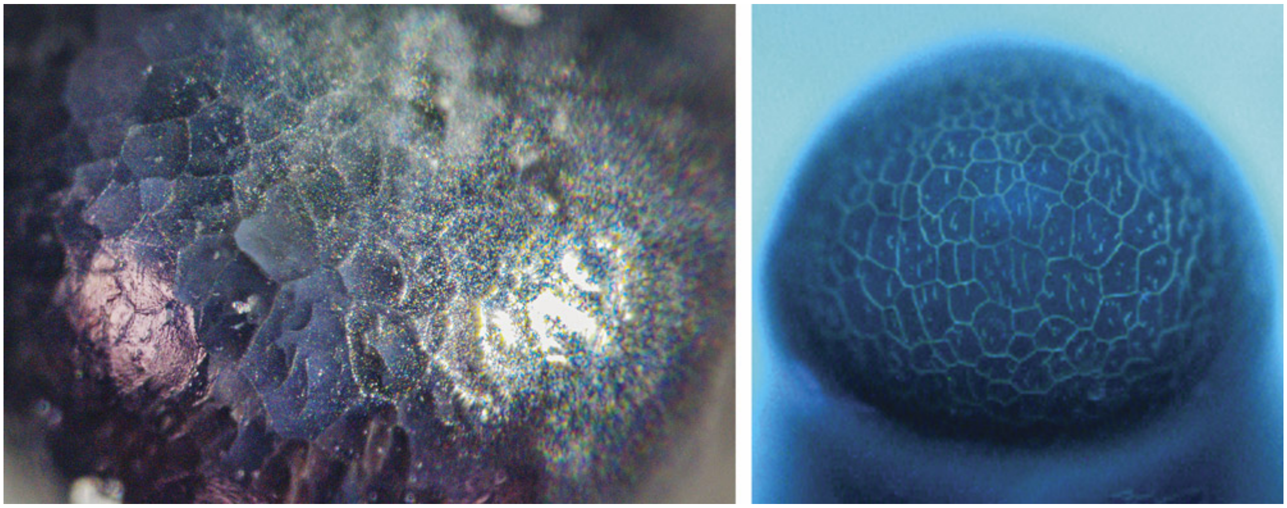

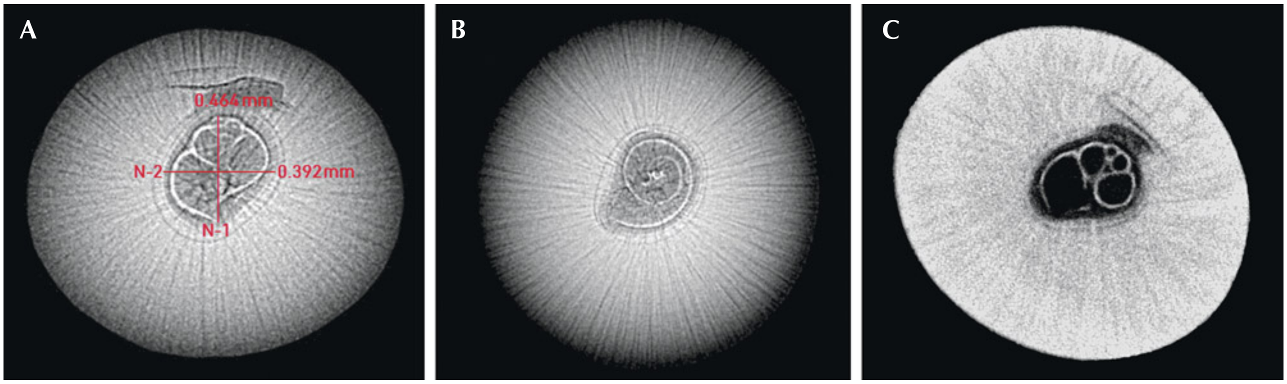

Figure 21. A: RTX image showing the measurements of the foraminifera shell at the center surrounded by an acicular structure. B: RTX image of the pearl along its length, revealing the spiral top formation of the foraminifera shell. C: µ-CT image of the foraminifera shell and acicular structure.

view, the RTX image showed the spiral shape of the shell's apex (figure 21B). Given its chamber shape and tiny size, the shell was identified as a foraminifera (K. Kimoto et al., "Precise bulk density measurement of planktonic foraminiferal test by X-ray microcomputed tomography," *Frontiers in Earth Science*, Vol. 11, 2023, article no. 1184671). Additionally, µ-CT scan images were rendered using specialized software (C. Zhou et al., "New 3-D software expands GIA's pearl identification capabilities," *GIA Research News*, May 13, 2016), which showed a clearer visualization of the external morphology of the foraminifera shell within the pearl (figure 22), as shown in the video at www.gia.edu/gems-gemology/fall-2024-gemnews-foraminifera-shell-in-natural-non-nacreous-pearl.

Black non-nacreous pearls from *Pinctada radiata* are extremely rare, and it is very uncommon to see such intriguing internal structures with foraminifera shells surrounded by acicular structures. The presence of this non-nacreous seed pearl with such a structure adds to GIA's comprehensive research database, contributing to the ongoing studies of unique formations found in natural pearls from the wild.

Abeer Al-Alawi, Anukul Belanke, Lubna Sahani, and Roxane Bhot Jain
GIA, Mumbai

Emiko Yazawa
GIA, New York

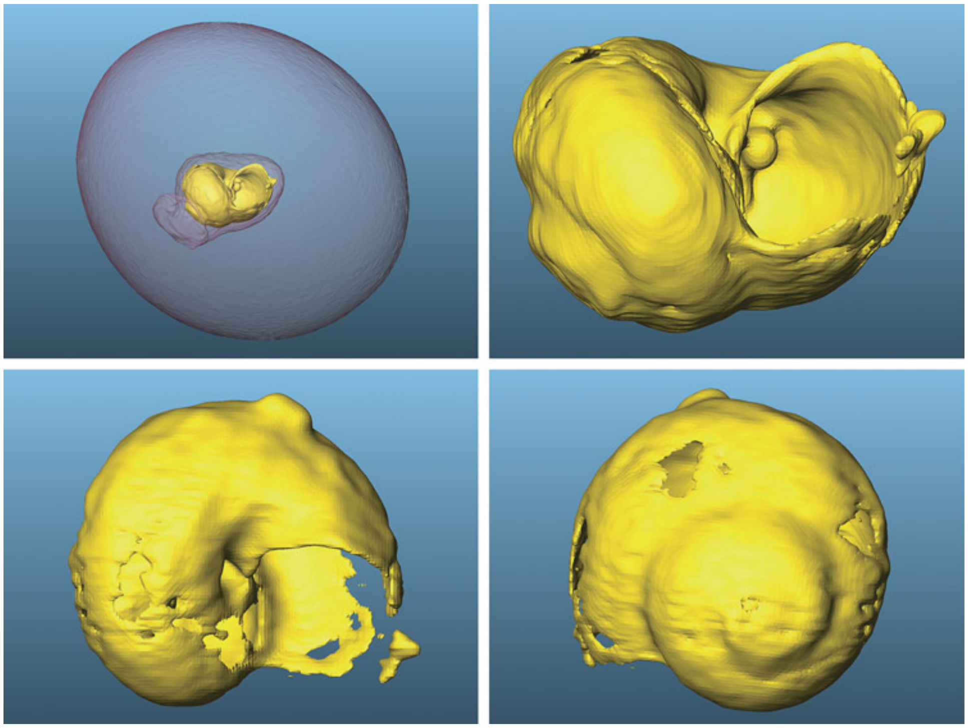

Figure 22. 3D images constructed from µ-CT scans showing the tiny foraminifera shell's morphology.

Figure 23. Left: This gourd-shaped saltwater bead cultured pearl (2.04 g and 15.90 mm high) displays two different colors. Right: Magnification indicates that the two parts grew together naturally. Photos by Yanhan Wu.

An unusual saltwater bead cultured pearl. A saltwater pearl with an unusual appearance was discovered in the pearl market in the city of Zhuji, in China's Zhejiang Province. It was shaped like a gourd, consisting of a silver gray part and a black part with green overtone (figure 23, left). The pearl's unusual color and shape raised suspicions about whether it had been artificially processed.

The pearl weighed 2.04 g and had a height of 15.90 mm. The gray part measured 6.79 × 6.12 × 5.07 mm and the black part 10.64 × 10.75 × 10.83 mm. Upon magnification, it appeared the two parts grew together naturally, rather than being artificially attached (figure 23, right).

No silver was detected with energy-dispersive X-ray fluorescence in either part, indicating that the pearl had not been treated with silver nitrate dye. The ultraviolet/visible/near-infrared (UV-Vis-NIR) reflectance spectra of both parts showed absorptions at 279, 405, 500, and 700 nm (figure 24, left), consistent with previous studies on the absorption of saltwater cultured pearls (S. Karampelas et al., "UV-Vis-NIR reflectance spectroscopy of natural-color saltwater cultured pearls from *Pinctada Margaritifera*," Spring 2011 *G&G*, pp. 31–35). In the visible light region, only the cause of the 405 nm band has been identified; it is attributed to a kind of porphyrin called uroporphyrin (Y. Iwahashi et al., "Porphyrin pigment in black-lip pearls and its application to pearl identification," *Fisheries Science*, Vol. 60, No. 1, 1994, pp. 69–71). The black part was more absorbed than the gray part due to its richer color.

The Raman spectra displayed bands at 1085 and 704 cm^{-1} (figure 24, right), corresponding to the ν_1 symmetric and the ν_4 in-plane bending modes of the carbonate ion (CO_3^{2-}) in aragonite (J. Unvros et al., "Characterization of

Figure 24. Left: The UV-Vis-NIR reflection spectra of the two parts of the pearl showed the same absorption positions and differences in intensity. Spectra are offset vertically for clarity. Right: Raman spectroscopy displayed the bands of aragonite and organic components.

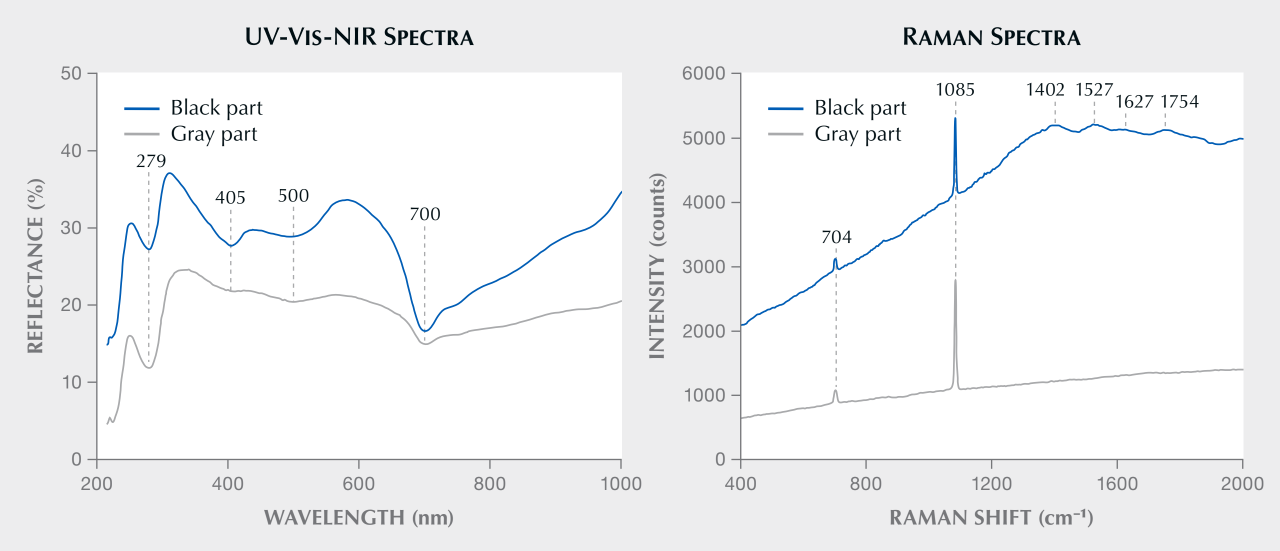

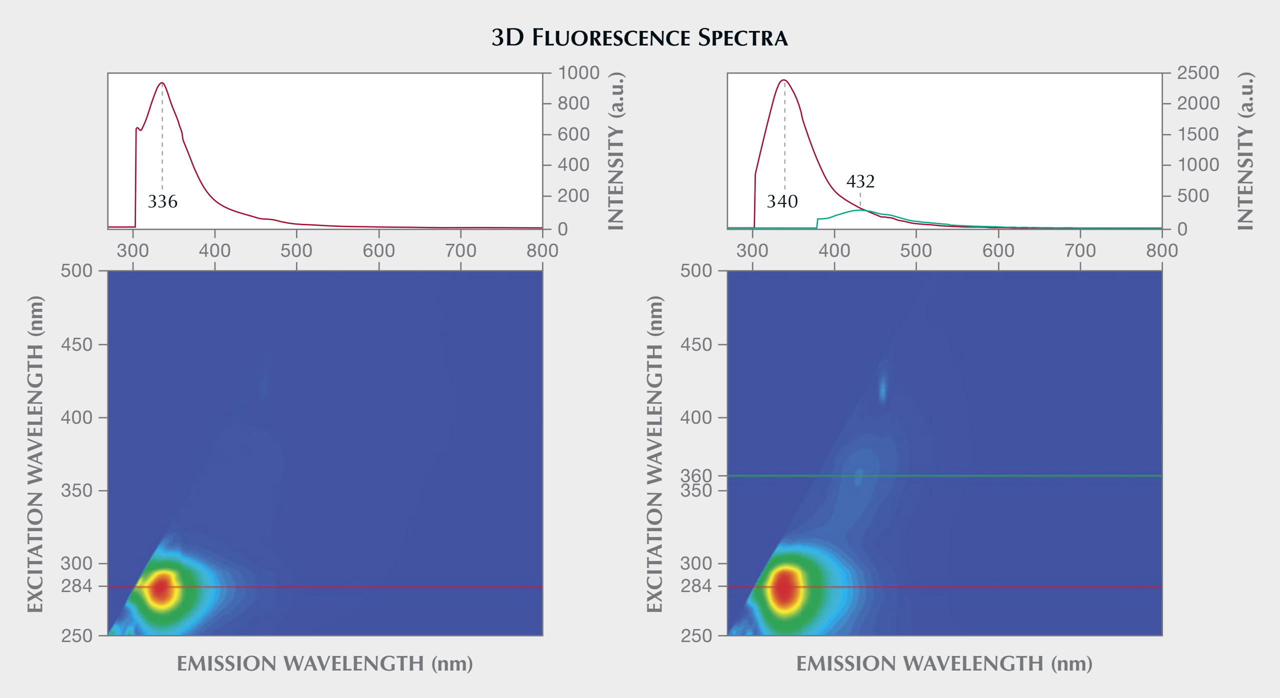

Figure 25. 3D fluorescence spectra of the black part of the pearl (left) and the gray part (right).

some biogenic carbonates with Raman spectroscopy," *American Mineralogist*, Vol. 76, 1991, pp. 641–646). Compared to the gray part, several broad bands were observed in the black part at 1800–1400 cm^{-1}, with centers at approximately 1754, 1627, 1527, and 1402 cm^{-1}. These Raman features were attributed to various types of organic components, such as conchiolin and porphyrin, and their intensity clearly increased with the color tone (W. Wang et al., "Identification of 'chocolate pearls' treated by Ballerina Pearl Co.," Winter 2006 *G&G*, pp. 222–235). These could exclude the possibility of irradiation treatment and other staining treatments.

Under long-wave ultraviolet radiation, both parts exhibited purplish blue fluorescence. However, the gray part exhibited significantly more intense fluorescence than the black part. The 3D fluorescence spectra confirmed this. The strongest fluorescence in the black part was at 336 nm (figure 25, left), while the strongest in the gray part was at 340 nm (figure 25, right). The fluorescence intensity between the two differed by more than 2.5 times. The gray part still had weak fluorescence centers at 432 nm, while the black part did not.

Although the study showed that the pearl's fluorescence may be attributable to the organic compounds contained within the nacreous layers (J. Hiramatsu et al., "Non-destructive assessment of the effects of heat and sunlight on akoya pearl quality," *Seibutsu Kogaku*, Vol. 88, No. 8, 2010, pp. 378–383), the cause of the different fluorescence characteristics is unknown.

The X-ray computed microtomography (µ-CT) scan in figure 26 shows that the outer layer of the two parts was connected by nacre, while the inner layer was composed of voids and organic components. Both parts had a distinct bead nucleus. The organic matter between the bead nucleus and the nacre had a dark gray circular shape. The nacre thickness in both parts was 3–4 mm.

Figure 26. µ-CT scan images of the saltwater bead cultured pearl at different depths.

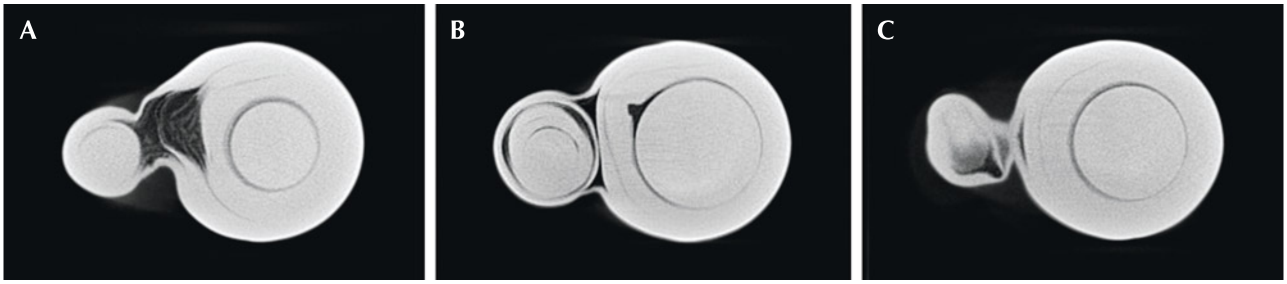

Many mechanisms combine to affect the color of pearls during their growth process (Z. Wang et al., "How cultured pearls acquire their colour," *Aquaculture Research*, Vol. 51, 2020, pp. 3925–3934), making it difficult to pinpoint the exact mechanism. This research can be used to further study the relationship between organic compounds and the color and fluorescence reactions of saltwater pearls, excluding variables such as mollusk type and environmental factors.

Yanhan Wu and Xianyu Liu
College of Jewelry, Shanghai Jian Qiao University

Yanling Yang
Sichuan University

New production of sapphire from Matepwende, Tanzania. In February 2024, Mark Saul (Amor Gems, Kenya) informed author VP about a sapphire rush near Matepwende village, located in the Namtumbo district in Songea, in southern Tanzania. News of a rush involving several thousand migrant miners from all around the country was soon publicized on Tanzanian television.

The following month in Bangkok, VP acquired a parcel of "F-type" reference samples (according to the GIA classification system) (W. Vertriest et al., "Field gemology: Building a research collection and understanding the development of gem deposits," Winter 2019 *G&G*, pp. 490–511; V. Pardieu, "Field gemology, the evolution of data collection," *InColor*, No. 46, 2020, pp. 100–106) reportedly from the new deposit for preliminary study (figure 27). Some were used for a heat treatment experiment in Thailand, and 27 others were sent to author AP for gemological study.

While samples were being studied at GIA, VP visited the new deposit in early June 2024 with geologists Leonard Cornuz and Yedidia Mgema. The site is in a remote area about five hours' drive from Songea using dirt roads during the dry season. It is 7 km north of the Ruvuma River bordering Mozambique. Geologically, it lies at the boundary between the Luwegu sedimentary sub-basin (part of the Selous basin) and the metamorphic Usagaran Belt. A uranium prospective license covers most of the deposit.

The deposit is a primary hard rock deposit where blue sapphires are associated with feldspar and mica in pegmatites intruding into gneisses (figure 28). Most of the sapphires are inside the pegmatites, while others are found in a mica-rich reaction zone between the pegmatite and the gneiss, indicating a desilicated pegmatite deposit (G. Giuliani et al., "The geology and genesis of gem corundum deposits," in L.A. Groat, Ed., *The Geology of Gem Deposits*, 2007, Mineralogical Association of Canada Short Course Series). Most of the mining activity occurred in the nearby detrital deposit over and near the pegmatites and in the limited secondary deposits along streams. The site of the rush covered approximately 1 square kilometer. About 400 artisanal miners (mostly from the Songea or Tunduru) were in the area during VP's visit, down from 1,000 a few weeks earlier at the height of the rush. About half were directly involved in mining, while the others were buying gems or providing supplies to the miners.

Figure 27. Blue sapphires from the Matepwende area in southern Tanzania. Most of the production consists of low-clarity material in matrix. Only a very small percentage (usually weighing less than 1 ct) is clean enough to be faceted. Photo by Vincent Pardieu.

The best facet-grade, fine-color sapphire seen during the expedition was a deep blue stone weighing about 2 ct, while the other fine stones were under 1 ct. We also saw kilos of heavily fractured and twinned corundum specimens up to 500 g, locally called "cabochons," that are broken to extract fragments of blue facetable material to be used for calibrated stones (figure 29). Most of these stones were industrial-, carving-, or bead-grade. According to locals, the deposit has been a known source of this material for more than 30 years. While some of the stones have an attractive blue coloration, most have a grayish overtone. Regarding clarity, most stones exhibit polysynthetic twinning and fractures, and more than half are also milky/silky. A heat treatment experiment under reducing conditions was conducted in Thailand by Karim Guer-

Figure 28. A: Large grayish blue sapphire crystals (about 5 cm) in white feldspar. B: Geologists check a sapphire-rich pegmatite in an artisanal mining excavation near Matepwende. C: A small deep blue facet-grade sapphire fragment within a heavily fractured sapphire crystal associated with (whitish) feldspar and (dark) mica. Photos by Vincent Pardieu.

chouche from Premacut Ltd. The stones did not improve with heat treatment.

Author AP used 12 sapphires from the deposit for a preliminary study, splitting the material into two groups

Figure 29. Left: Two miners with kilos of sapphire rough. Right: The result of their work after breaking the heavily fractured sapphires into attractive parcels of small sapphire. Photos by Vincent Pardieu.

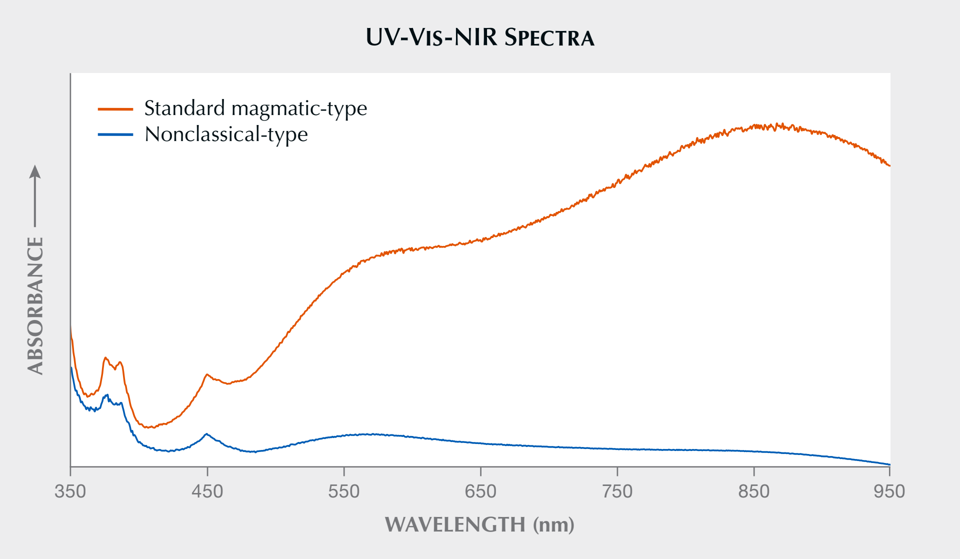

Figure 30. Representative UV-Vis-NIR spectra of Matepwende sapphire. Half of the samples showed a standard magmatic-type UV-Vis-NIR spectrum with a prominent 880 nm band and Fe^{3+}*-related features, while the other half showed a nonclassical spectrum without a prominent 880 nm band but with prominent Fe*$^{3+}$*-related features.*

based on their ultraviolet/visible/near-infrared (UV-Vis-NIR) spectra (figure 30). One group of six samples had UV-Vis-NIR spectra more typically seen in basalt-related sapphires, such as those from Australia or Thailand, with a prominent broad band absorption at 880 nm and significant Fe^{3+}-related features at 377, 388, and 450 nm. These are often called "magmatic-type" or "CMG" sapphires. The other group of six samples lacked the prominent 880 nm band but still had significant Fe^{3+}-related features. These are often called "nonclassical" (NCL) sapphires, and they include sapphires from Montana in the United States and both Umba and Songea in Tanzania.

The inclusion characteristics were different between these groups. The CMG-type sapphire from Matepwende generally displayed platelet-type inclusions and reflective silk that appeared white under strong fiber-optic light (figure 31). Twinning was also common in this group. The NCL-type sapphire from Matepwende, on the other hand, had reflective silk, sometimes in linear bands or stringer-type inclusions that appeared brassy or yellow with reflected fiber-optic light (figure 32). In these NCL-type Matepwende sapphires, the silk also took on a grayish cast with transmitted brightfield light.

Despite these differences, the trace element chemistry of both groups was very similar and matched more closely with that expected of basalt-related blue sapphire, with relatively low magnesium and elevated iron and gallium (table 1). Fourier-transform infrared (FTIR) spectra for both groups were also very similar. All the sapphires had a prominent 3309 cm^{-1} peak and a pair of peaks at 3394 and 3379 cm^{-1}. A few samples showed the presence of boehmite in FTIR as well. The difference in UV-Vis-NIR spectra between these two groups was unexpected, given that they were reportedly from the same deposit. The authors had never witnessed such a case, where a single geographical locality produced sapphires displaying two distinct types of UV-Vis-

Figure 31. Platelet-type inclusions (left) and reflective silk (right) in the Matepwende sapphires with a magmatic-type UV-Vis-NIR spectrum. Photomicrographs by Aaron Palke; fields of view 1.58 mm (left) and 1.26 mm (right).

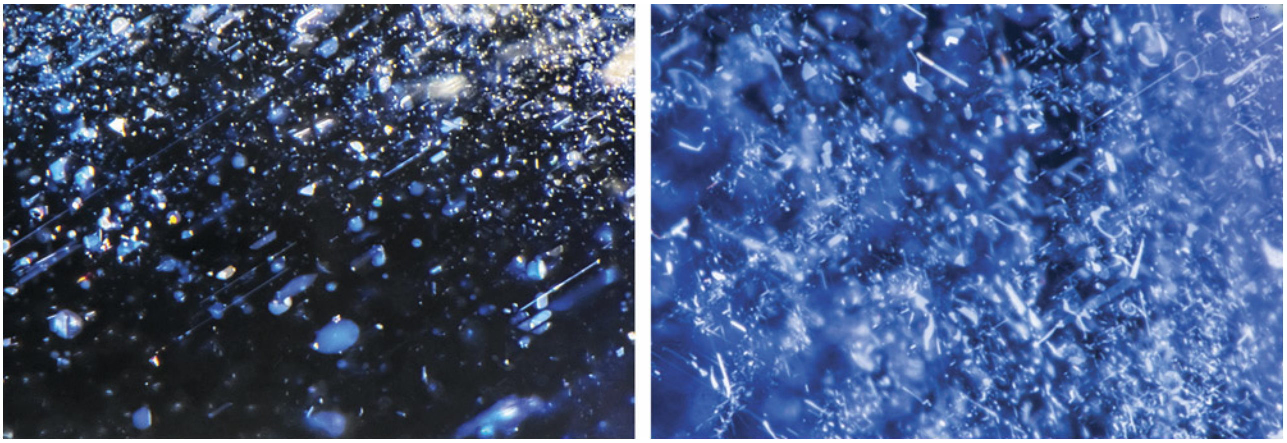

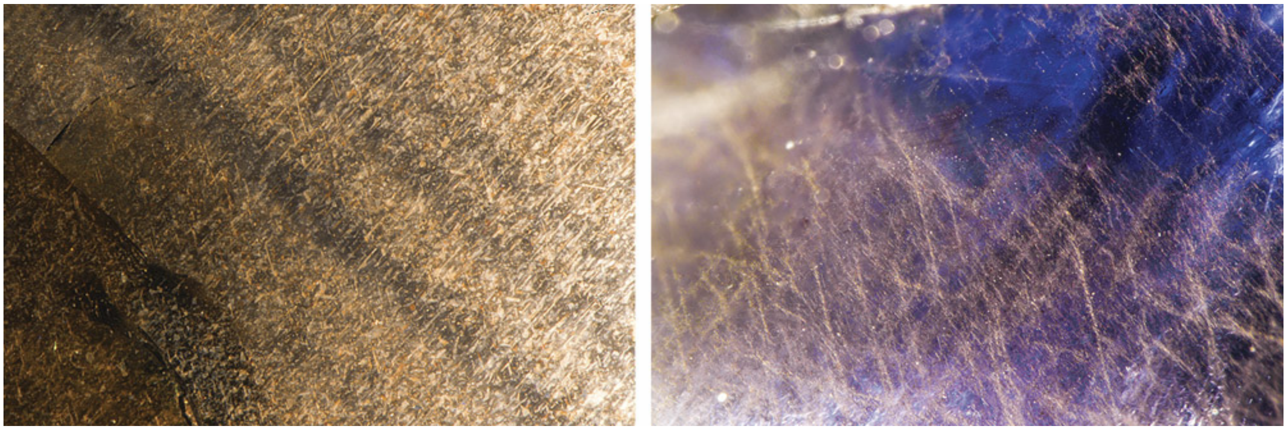

Figure 32. Bronzy reflective silk in dense linear bands (left) and as stringers (right) in the Matepwende sapphires with a nonclassical-type UV-Vis-NIR spectrum. Photomicrographs by Aaron Palke; fields of view 1.99 mm (left) and 2.90 mm (right).

NIR spectra. However, the similarity in trace element chemistry and FTIR spectra suggests a genetic link between these two groups of sapphire from Matepwende. Based on observations during the visit to the deposit, one possible explanation is that the CMG sapphires could have formed inside the pegmatite, while the NCL samples could have formed inside the reaction zone. A study of the material collected at the mine from the pegmatites and reaction zones could help to confirm this hypothesis.

Aaron Palke
GIA, Carlsbad

Vincent Pardieu
VP Consulting WLL, Bahrain

DIAMONDS

Master diamond cutter Harvey Lieberman. For half a century, Harvey Lieberman has perfected the subtle art of cutting colored diamonds and bringing out their vivid hues and tones. Lieberman, nearing retirement, has sat at the same cutting bench (formerly his father's bench) for 35 years in the renowned William Goldberg diamond cutting factory (figure 33). Goldberg (1925–2003) was a legend in his own right, often hailed as the father of New York's Diamond District.

Lieberman is part of an elite community at the Goldberg cutting factory. Any given week might find Mutty Bornstein, Willy Lopez, Shmiel Wurzberger, or Eliezer Gottlieb at work. Each is a master cutter of both colorless and colored diamonds. Their camaraderie and shared passion for the craft make the factory a thriving hub of expertise and collaboration.

Lieberman graduated from Queens College in New York with a theater arts degree in 1974. He planned to wait tables, audition, and chase that big break. (Lieberman still does some occasional acting in off-Broadway productions.) But his father, being practical, told him, "Let me at least

TABLE 1. Trace element concentrations (in ppma) of Matepwende sapphires, measured by LA-ICP-MS.

	Mg	Ti	V	Cr	Fe	Ga
Sapphire with magmatic UV-Vis-NIR spectra						
Range	0.24–8.64	1.6–9.5	0.3–1.7	0–9.33	1190–1588	26.8–35.7
Average	2.02	5.57	0.88	3.80	1321.78	32.52
Median	0.57	4.90	0.82	2.75	1272.50	33.05
Sapphire with nonclassical UV-Vis-NIR spectra						
	Mg	Ti	V	Cr	Fe	Ga
Range	0.51–2.62	5–25	0.69–2.93	0.49–4.12	1103–1603	27.8–50.3
Average	1.11	10.39	1.43	1.55	1366.33	35.37
Median	0.60	7.90	0.75	0.85	1397.00	29.65
Detection limit (ppma)	0.01	0.03	0.002	0.04	0.59	0.001

Figure 33. Harvey Lieberman at the diamond cutting bench where he has worked for the past 35 years—the same bench his father used before him. Photo by Pedro Padua.

teach you a trade." And with that, Lieberman apprenticed with his father, a master cutter on West 47th Street, learning the intricacies of cutting colorless diamonds.

His introduction to the craft at age 24 was cutting macles (twinned diamonds). Lieberman struggled with these uncooperative diamonds, whose crystal structures are knotted, watching as they ruined one cutting wheel after another. It was difficult, frustrating work. After nearly a year, he quit. He spent the next two years traveling, trying to sell gold and diamonds to jewelers, but it was not his calling. After two years of false starts, Lieberman returned to his father's side, ready to give diamond cutting another shot. This time, though, he was armed with a better attitude and much more patience.

When his father became the foreman at Goldberg's cutting factory, he brought Harvey along. The senior Lieberman did more than just cut and polish; he traveled to London, granted the rare privilege of attending De Beers sights. These were exclusive events where only a handful of companies could purchase rough diamonds directly from De Beers. Harvey joined him and had a front-row seat to the inner workings of the diamond industry, from the raw power of uncut gems to the dazzling brilliance of a perfectly cut stone. This became his world.

Everything changed when Lieberman first laid eyes on colored diamonds brought to him by his uncle, who had worked with the renowned Stanley Doppelt and Louis Glick. Doppelt and Glick would take in the yellow rough, painstakingly cutting it into smaller pieces to downplay the color. But his uncle had a different vision. He began cutting to maximize the color, pioneering a new market for vibrant yellow diamonds. This was Lieberman's introduction to the magic of amplifying color through cutting.

Initially it was trial and error, and each stone was a new test—especially regarding the delicate pinks. One prominent dealer who sourced pink diamonds from Argyle would bring them to Lieberman to bring out the color. With that, Lieberman embarked on a journey to unlock the full potential of colored diamonds. Improving the color grade from intense to vivid became a goal. One time, Lieberman received an Argyle 2.14 ct Fancy Deep pink. After cutting it, he ended up with a stone just under 2 carats that had transformed into a pure red. The value improved nearly tenfold.

Lieberman worked under his father for a while and then for Louis Glick, who sent him to a De Beers sight and tenders in Africa (where non–De Beers mines sell rough diamonds, some in remote armed compounds). He was then assigned to start a factory in Africa. After a few years, he brought his family back to the U.S. and rejoined Goldberg, who had kept the same bench for Harvey after his father passed away.

Lieberman has since worked with blues (figure 34 and figure 35, left), pinks (figure 35, right), reds, greens, and others. He has made color grades go from light to intense, all by changing how the diamond is cut. In the world of diamonds, color is everything. And improving that color is an art form few have mastered. Lieberman is one of the

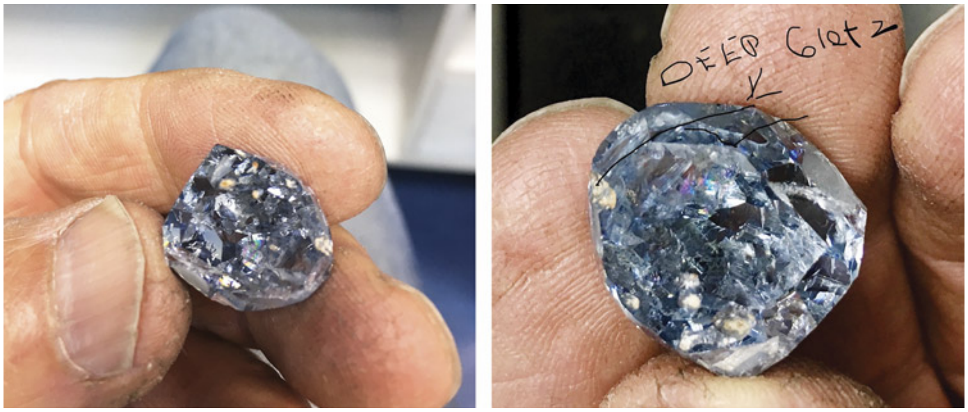

Figure 34. Lieberman examines a 40 ct rough blue diamond that yielded a 15 ct heart. The lines on the right photo indicate where the stone might be sawn. Photos courtesy of Harvey Lieberman.

Figure 35. Left: The 15 ct vivid blue heart-shaped diamond cut from the rough shown in figure 34. Right: A 9 ct vivid pink and a 5.5 ct deep pink cut by Lieberman. Photos courtesy of Harvey Lieberman.

select few. With years of experience, he has transformed diamonds of all kinds, bringing out their hidden beauty. But sometimes, he looks at a diamond and has to tell the owner it cannot be improved. That candor makes his expertise especially valuable.

The works of Lieberman and his Goldberg factory collaborators have graced the halls of the Smithsonian (including the 5.1 ct Moussaieff Red diamond) and been highlighted at numerous auctions. One was a 1.92 ct Fancy red radiant cut diamond with VS_2 clarity, the second most expensive red per carat at the time, sold at a Phillips New York auction. The Pumpkin diamond, a 5.54 ct Fancy Vivid orange cushion cut, was bought by Harry Winston at a Sotheby's auction. These are just a few of their masterpieces.

This interview with Harvey Lieberman was captured on video as part of GIA's Oral History Project to be used by future historians. To see more, go to www.gia.edu/gems-gemology/fall-2024-gemnews-harvey-lieberman.

Al Gilbertson
GIA, Carlsbad

"Out of the Darkness"…and into the light of diamond fluorescence. GIA's Carlsbad laboratory recently had the opportunity to examine "Out of the Darkness," a diamond art piece created in 2021 by South African artist Johnathan Schultz (figure 36). This unique design hosting 9,225 diamonds, totaling just over 895 carats, is laid out as a reproduction of Nelson Mandela's fingerprint (figure 37). The representation measures approximately 20 × 15 in. (51 × 38 cm). Schultz incorporated gold and diamonds in the piece as an homage to some of his home country's most valuable resources. According to the artist, all of the diamonds are round brilliants with G–H color and VS or better clarity. Each was mounted in a white gold martini setting with the posts removed. The mounted diamonds were then soldered together to produce the ebbs and flows of the individual lines in the fingerprint. Using a few carefully selected posts that were left in place, the strands were attached to clear acrylic in just the right pattern to replicate one of Mandela's fingerprints preserved from his 1962 arrest.

Figure 36. Artist Johnathan Schultz working on "Out of the Darkness," a reproduction of Nelson Mandela's fingerprint with more than 9,200 diamonds set in white gold. Photo by Michael Craigwood; courtesy of Johnathan Schultz.

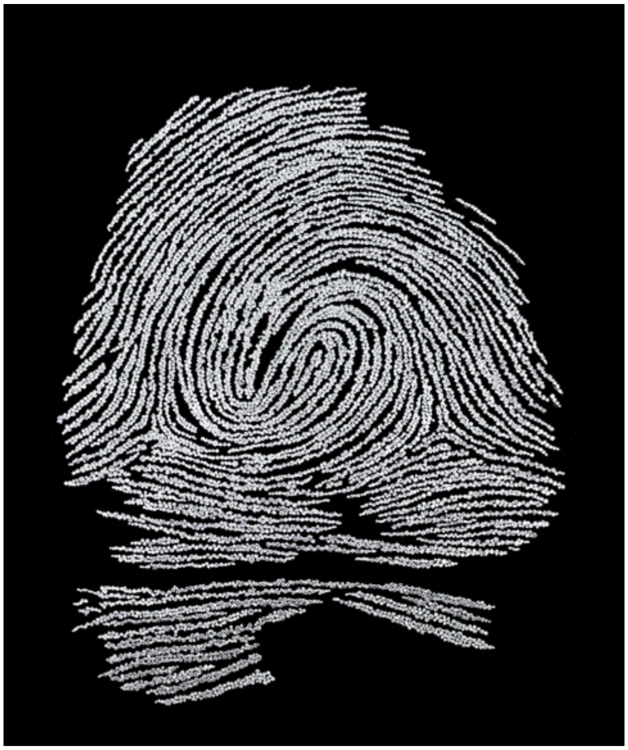

Figure 37. Johnathan Schultz's "Out of the Darkness" contains 9,225 diamonds laid out in an artistic representation of Nelson Mandela's fingerprint. The fingerprint measures approximately 20 × 15 in. (51 × 38 cm). Photo by Rhonda Wilson and Annie Haynes.

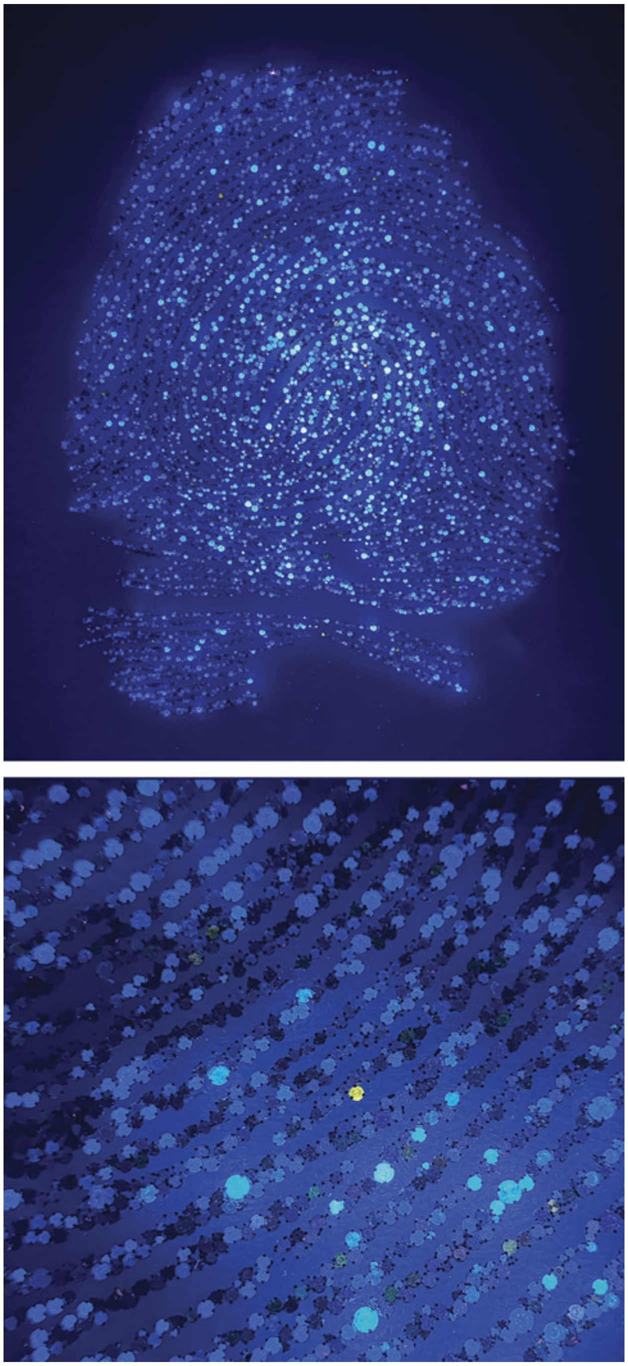

Figure 38. The fluorescence reaction of the diamonds under long-wave UV (365 nm excitation). Photos by Christopher M. Breeding.

While the work itself is extraordinary and among the largest diamond art pieces ever made, it also provided GIA with an excellent opportunity to employ testing and instrumentation in rare and challenging ways. Testing small mounted diamonds to determine if they are natural or laboratory-grown is never easy, but when attached in such large numbers in a fragile and valuable art piece, the challenge is magnified. Using the flexible instrument probe of the GIA iD100, the subset of diamonds examined were identified as natural. The iD100 uses the fluorescence properties of natural diamonds to accurately and conclusively determine their natural origin.

During testing, Schultz was introduced to a different aspect of his art: the beauty of diamond fluorescence. A handheld long-wave LED ultraviolet light revealed the array of color hidden in the fingerprint produced by the fluorescence of the diamonds (figure 38). While mostly blue due to nitrogen atoms in the diamond structure, the diamonds' fluorescence colors also included some yellow, orange, pink, whitish, and greenish glowing hues. The combination made for a spectacular, almost night-sky appearance that seemed to inspire creative ideas for his next endeavor with diamonds.

Using innovative technology and expertise, we were able to not only identify the nature of the diamonds in this art piece but also offer the artist a new perspective, showing that the beauty of diamond is further enhanced by the science of diamond.

Christopher M. Breeding
GIA, Carlsbad

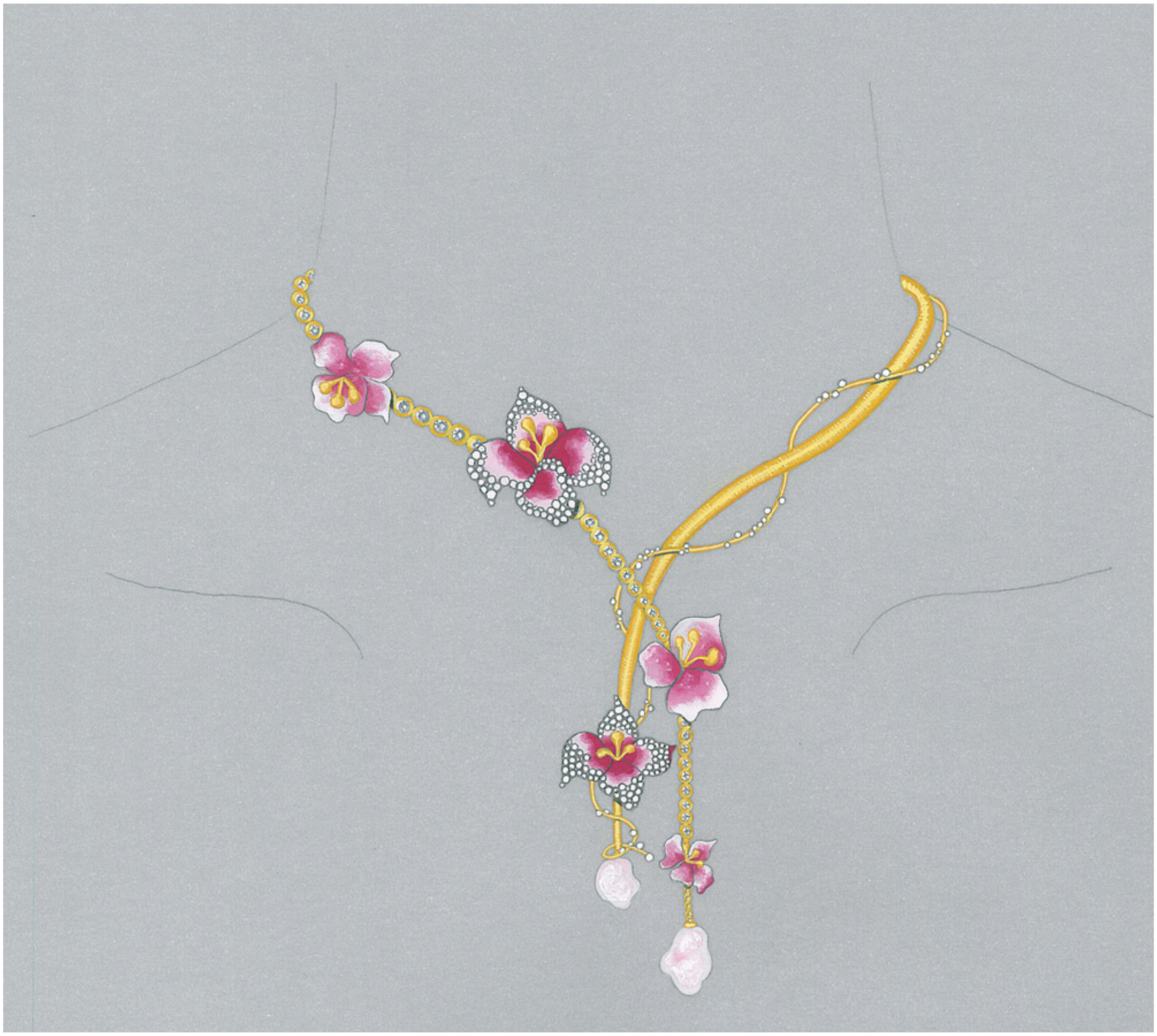

Figure 39. Srushti Shah's design sketch for a necklace featuring 18K yellow gold, baroque pearls, diamonds, light pink garnets, and colored glass enamel.

JEWELRY DESIGN

GIA student design showcase. One of GIA's "student choice" awards was recently presented to Srushti Shah, a graduate of the Jewelry Design program at the London campus. Shah's design combines 18K yellow gold, baroque pearls, diamonds, light pink garnets, and colored glass enamel to create a vine of cherry blossoms draped around the neck (figure 39). Shah noted, "This necklace design draws on the symbolism of cherry blossoms, embodying the cycle of life and generational connections. The five cherry blossoms on the necklace represent significant milestones in the journey of life, inspired by Antoine de Saint-Exupéry's *The Little Prince*. Diamonds reflect the wonder of childhood. The gold vines capture the exploration and learning that shape our growth. Freshwater pearls, symbols of wisdom gained through life's experiences, represent love and relationships. Enamel brings the blooms to life, echoing resilience in facing life's challenges. Baby pink garnets in the flowers evoke the gentle hues of spring, celebrating reflection and legacy."

SYNTHETICS AND SIMULANTS

"Cotton pearl" imitations. For centuries, pearls have been one of the most imitated gems. Traditionally created by coating spherical glass beads with pearlescent paint, these

Figure 40. Left: A variety of cotton pearls imitating akoya, golden South Sea, and Tahitian pearls. Right: A necklace featuring pistachio-colored cotton pearls. Photos by Annie Haynes.

imitations were designed to resemble the color, luster, and heft of genuine pearls. This continued with the advent of plastic beads and, more recently, coated shell beads (Summer 2014 Lab Notes, pp. 153–154). A new simulant has since been gaining popularity in the fashion jewelry market: "cotton pearls" (figure 40).

Cotton pearls are available in a variety of colors and sizes, allowing them to imitate nearly every pearl species. These beads are created from cotton fibers or other fibrous textile materials that are tightly packed and concentrically layered. Their internal structure can be revealed by real-time X-ray microradiography (RTX), as shown in figure 41. The image displays concentric bands composed of fine fibers as well as a bright white edge representing the higher-density coating on the bead's exterior. The star-shaped "drill hole" is likely a remnant of the manufacturing process rather than an actual drill hole. It is possibly in the shape of the spindle on which the fibers are rotated, creating concentric layering. To examine the interior, a bead was cut in half perpendicular to the "drill hole." This

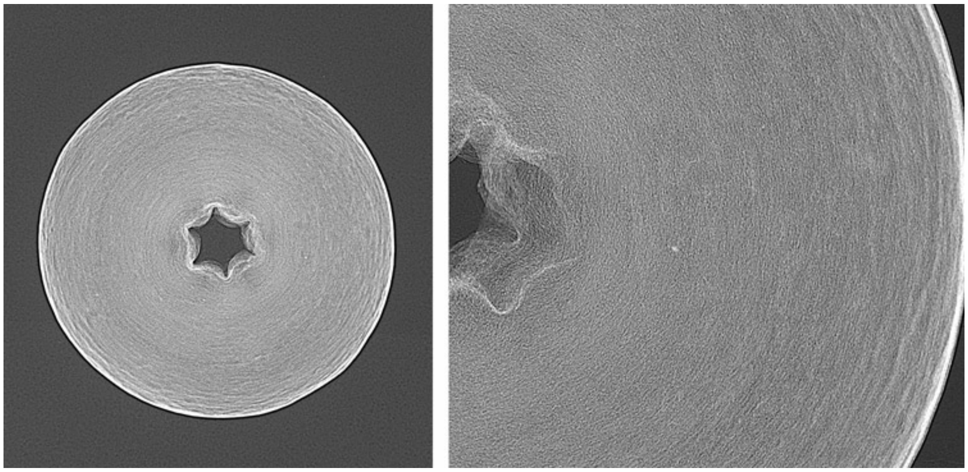

Figure 41. Left: RTX image of a cotton pearl featuring a star-shaped center hole, likely a manufacturing remnant. Fine concentric banding can be seen along with a bright white outer edge representing the higher-density surface coating. Right: A closer view of the bead reveals a fine fibrous texture.

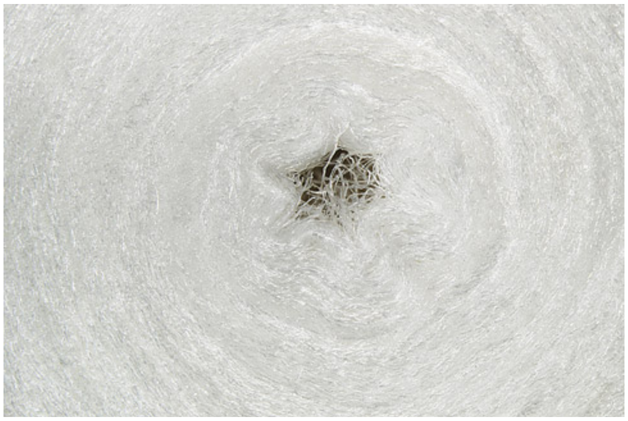

Figure 42. *A cross section of a cotton pearl viewed perpendicular to the "drill hole." Fine white fibers with a concentric layered structure were observed throughout the interior, resembling what was seen in the RTX image. Photomicrograph by Britni LeCroy; field of view 7.19 mm.*

exposed tightly packed white fibers throughout with faint concentric layering (figure 42), consistent with observations from the RTX images.

Cotton pearls are lightweight and comfortable to wear, particularly compared to glass or shell imitations of large pearls such as South Sea or Tahitian. They are also surprisingly strong and did not deform when pressed firmly between the fingers. Additionally, the textured surface of cotton pearls gives them a convincing visual impression.

If imitation is the sincerest form of flattery, then pearls certainly continue to inspire admiration and innovation.

Britni LeCroy
GIA, Carlsbad

Pearls marketed as "Venezuelan pearls." The term "Venezuelan pearls" is applied to natural saltwater pearls harvested from the *Pinctada imbricata* mollusk, also known as the Atlantic pearl oyster. They are found primarily in the western Atlantic, from Bermuda and Florida to northern South America. The mollusk size ranges from 5 to 7 cm and produces pearls ranging from less than 2 mm (seed pearls) up to 9 mm (*CIBJO Pearl Guide*, 2022). Some traders claim that many pearls sold as "Venezuelan pearls" in the world markets today, mainly India and the Middle East, are sometimes mixed with pearls from other *Pinctada* species (typically lower- to medium-quality *Pinctada maxima* pearls). Others claim that actual pearls from Venezuela are also sold as "Basra pearls," which are sourced from *Pinctada radiata* and are highly valued in India and the Middle East due to their appearance and luster.

GIA's Mumbai laboratory studied a parcel of 988 reportedly "Venezuelan pearls" from one of the main suppliers of this material (figure 43). The internal structures were examined with real-time X-ray microradiography (RTX),

Figure 43. A lot of pearls sold as "Venezuelan pearls," ranging from 2.05 × 1.88 mm to 6.87 × 5.23 × 4.23 mm. Photo by Gaurav Bera.

and 97 samples were selected for further study. The majority of the button-shaped and semi-baroque pearls were white to light cream and cream in color, and most exhibited strong orient. Their weight ranged from 0.05 to 1.06 ct, with sizes from 2.05 × 1.88 mm to 6.87 × 5.23 × 4.23 mm. Most of the samples exhibited a good luster with a smooth surface, and a few revealed minor surface blemishes. Under high magnification, the samples showed various patterns of overlapping aragonite platelets on the surface, which are typically observed in nacreous pearls.

Energy-dispersive X-ray fluorescence on the 97 selected samples revealed low manganese levels ranging from below detection limit to 29 ppm, with a few ranging from 32.5 to 69.8 ppm. Higher strontium levels were also observed, from 1177 to 2988 ppm, with a few samples ranging from 3056 to 3437 ppm. When exposed to X-ray fluorescence, most of the samples showed an inert reaction, while a few exhibited an extremely faint yellowish green reaction. Under long-wave ultraviolet radiation, all the pearl samples luminesced various degrees of bluish green.

Raman spectroscopy revealed a doublet at 701/704 cm^{-1} and a peak at 1086 cm^{-1}, with a few pearls showing a weak peak at 1464 cm^{-1} indicative of aragonite. Additionally, the spectra of one light cream and one cream pearl showed weak polyenic pigment peaks at 1135 and 1530 cm^{-1}. These observations were previously documented for pearls from *Pinctada fucata* (akoya) and *Pinctada radiata* (A. Al-Alawi et al., "Saltwater cultured pearls from *Pinctada radiata* in Abu Dhabi (United Arab Emirates)," *Journal of Gemmology*, Vol. 37, No. 2, 2020, pp. 164–179). Due to the pearls' smaller size, ultraviolet/visible/near-infrared spectra were collected for only 54 of them. Some of these displayed weak bands around 320, 395, and 420 nm, while others showed a prominent feature at 460 nm, similar to previously studied samples from *Pinctada imbricata*.

RTX analyses revealed a combination of structures that were typical of those observed in natural pearls from *Pinctada* species, as shown in figure 44. In this study, around 44% of the pearls revealed faint gray dense cores surrounded by growth arcs and organic-rich gaps at their outer edges. The samples displayed tight and minimal internal growth structures, some with thicker concentric growth arc formations following the shape of the pearl, representing approximately 16% of the group. Additionally, around 13% showed multi-nuclei structures, exhibiting a combination of different types of cores, while a few revealed interesting crystalline structures.

The most challenging to identify were void structures and linear features, which were found in only 6% of the samples. Some of these were long features that, to some extent, mirrored the outline of the pearl. The linear features originated from the tip of the pearls and were surrounded by a few growth arcs. These were similar to the odd linear structures observed in natural pearls from various mollusk species in GIA's research database. A total of 18% of the pearls revealed irregular centrally positioned voids of varying sizes. Voids are frequently observed in saltwater non-bead cultured (NBC) pearls, particularly those from *Pinctada* species. Therefore, it was important to further study these samples using X-ray computed microtomography (μ-CT) imaging, which indicated that many voids were filled with fine, light gray organic-rich matter, unlike the empty voids typically observed in NBC pearls

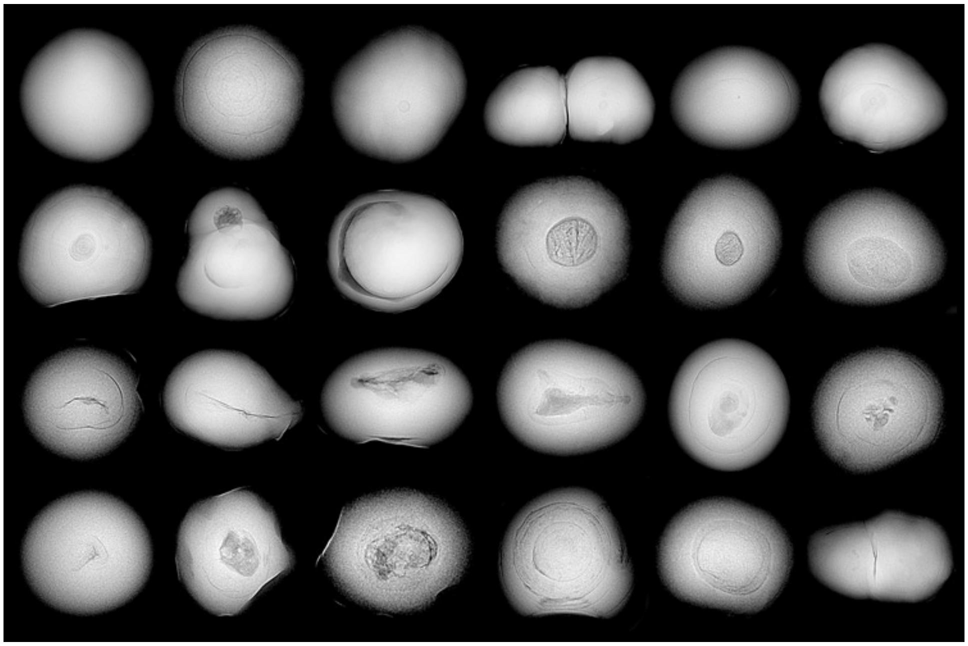

Figure 44. RTX imaging of various structures examined in the lot. The first row displays pearls with growth arcs and small faint cores, the second row shows different cores and crystalline structures, and the third row presents various linear and void features. The bottom row shows voids filled with organic matter, pearls with growth arcs, and faint cores in the multi-nuclei structure.

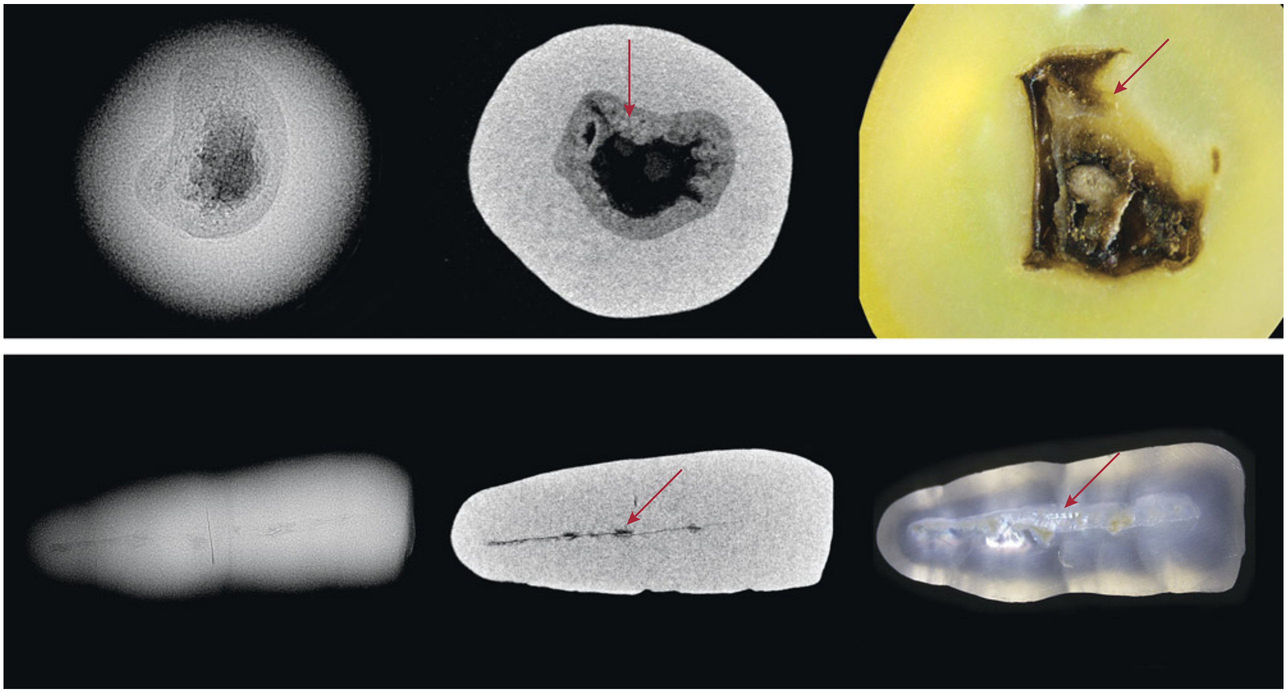

Figure 45. Left to right: RTX images, μ-CT images, and photomicrographs of two cut pearls. Top: Pearl A reveals a complex irregular void feature surrounded by an organic-rich area (arrow). Bottom: Pearl B exhibits an elongated linear structure with a knot-like feature (arrow). Photomicrographs by Karan Rajguru; field of view 1.3 mm and 3 mm, respectively.

(A. Homkrajae et al., "Internal structures of known *Pinctada maxima* pearls: Cultured pearls from operated marine mollusks," Fall 2021 *G&G*, pp. 186–205).

To further study these challenging internal structures, two pearls were ground down. The dark gray void-like area seen in the RTX image of pearl A was composed of a solid organic material that appeared as a light and dark brown area in the cross section (figure 45, top row). Pearl B, which showed an elongated linear structure in the RTX image, had a hollow space with organic-rich pockets (figure 45, bottom row).

Based on comparison with research samples from GIA's database, some of the samples from this lot had internal structures similar to those from *Pinctada imbricata*, but others displayed overlap with structures found in *Pinctada radiata* and *Pinctada maxima*. Although a few samples showed borderline void and linear internal structures, similar to NBC pearls from *Pinctada maxima*, the majority had structures seen in natural pearls from the other *Pinctada* species. These findings suggest that the potential mixing of these pearls, whether intentional or accidental, may be attributed to their remarkably similar external appearance. Consequently, more advanced testing utilizing laser ablation–inductively coupled plasma–mass spectrometry will be necessary to effectively differentiate between the pearls from the different *Pinctada* species mollusks mixed within the studied lot of pearls. Therefore, GIA's ongoing research serves as a valuable resource for identifying pearls from different mollusks.

Karan Rajguru, Abeer Al-Alawi, Gauri Sarvankar, and Roxane Bhot Jain
GIA, Mumbai

CONFERENCE REPORTS

IJK 2024. International Jewellery Kobe (IJK), held at the Kobe International Exhibition Hall every spring, is one of the premier international jewelry trade shows in the Kansai region of western Japan. Since Kobe is known for its pearl industry, pearl dealers exhibited in more than 100 booths out of 441 total. Overall, the show drew nearly 14,000 visitors.

Many vendors exhibited akoya bead cultured pearls, mostly in 6–8 mm sizes. With unusually large akoya bead cultured pearls from 11.0 to 12.2 mm seen at the Tucson show earlier this year (Summer 2024 GNI, pp. 255–256), the authors searched for similar sizes but only found them as large as 9.0–9.5 mm (figure 46). Some dealers said that 11 mm would be the largest size found at the show.

Meanwhile, small sizes (less than 10 mm) of Tahitian and golden South Sea bead cultured pearls are currently on

Figure 46. A strand of akoya pearls and a pair of earrings ranging in size from 9.02 to 9.49 mm. Photo by Asumi Sanbonmatsu; courtesy of Kuwayama.

the market (figure 47). The smallest Tahitian at the show was 7 mm, and the smallest golden South Sea pearl was 8 mm. The small Tahitian pearls featured various shapes, colors, and overtones, with very good to excellent luster, and some pits and blemishes on the surface (figure 47, left). According to one salesperson, these small Tahitian pearls

Figure 47. Tahitian pearl strands in 7–9 mm size (left) and golden South Sea pearl strands in 8–10 mm size (right). Photos by Moemi Ogawa; courtesy of Tanaka Pearl.

Figure 48. A conch pearl necklace offered at IJK. Photo by Asumi Sanbonmatsu; courtesy of Fiore Y.A.C.

were from the Philippines. He noted that pearl farmers are producing small Tahitian and golden South Sea pearls due to an unprecedented increase in demand. However, high-quality small pearls are still rare. On the other hand, very few South Sea white pearls were found below 10 mm in diameter, which might suggest a low demand due to the availability of akoya.

One vendor offered uniquely designed conch pearl jewelry (figure 48). These conch pearls had typical porcelaneous structures such as granulate, silk, and the highly prized flame structure.

The next IJK show will be held May 15–17, 2025.

Moemi Ogawa and Asumi Sanbonmatsu
GIA, Tokyo